

¹ **MicroBooNE: Neutron Induced Cosmogenic π^0 s**

² **Ryan A.Grosso**

³ Submitted in partial fulfillment of the

⁴ requirements for the degree

⁵ of Doctor of Philosophy

⁶ in the Graduate School of Arts and Sciences

⁷ **UNIVERSITY OF CINCINNATI**

⁸ 2018

9

10

©2018

11

Ryan A.Grosso

12

All Rights Reserved

¹³ Table of Contents

¹⁴	List of Figures	iii
¹⁵	List of Tables	v
¹⁶	1 Introduction	1
¹⁷	2 Neutrinos & Neutrino Oscillations	3
¹⁸	2.1 The History the Neutrino	3
¹⁹	2.2 Discovery of the Neutrino	5
²⁰	2.3 Neutrinos in the Standard Model	8
²¹	2.4 Neutrino Interactions	9
²²	2.5 Neutrino Mass and Flavor Oscillations	12
²³	2.6 Sterile Neutrinos	17
²⁴	3 The MicroBooNE Detector	18
²⁵	3.1 Brief History of LAR-TPC's	18
²⁶	3.2 Introduction	19
²⁷	3.3 Time Projection Chamber	20
²⁸	3.4 Light Collection	26
²⁹	3.5 Electronics Readout	28
³⁰	4 Booster Neutrino Beam	30
³¹	4.1 Primary Beam, Target and Horn	31
³²	4.2 Neutrino Flux Prediction	32

³³	5 Low Energy Excess and Relevant Cross Sections	35
³⁴	5.1 Overview	35
³⁵	5.2 LSND Excess	35
³⁶	5.3 MiniBooNE Excess	37
³⁷	5.4 Neutral Current π^0 production	38
³⁸	5.5 NC- π^0 in Carbon vs Argon	40
³⁹	6 Cosmogenic π^0s at MicroBooNE	41
⁴⁰	6.1 Motivation	41
⁴¹	6.2 Traditional Reconstruction	43
⁴²	6.3 Wire Cell Imaging	44
⁴³	6.4 Pattern Recognition	45
⁴⁴	6.5 Clustering	46
⁴⁵	6.6 Track and Shower Selection	48
⁴⁶	6.6.1 Track Removal	48
⁴⁷	6.6.2 Single π^0 Reconstruction	48
⁴⁸	6.7 Single π^0 cosmic sample	52
⁴⁹	7 Results	56
⁵⁰	7.1 Monte Carlo Simulation	56
⁵¹	7.2 Data	59
⁵²	7.3 Data-Monte Carlo Comparison	59
⁵³	8 Conclusions	62
⁵⁴	8.1 Conclusion	62
⁵⁵	I Appendices	63
⁵⁶	Bibliography	66

⁵⁷ List of Figures

58	2.1 Cowan and Reines first proposed neutrino experiment.	5
59	2.2 The hadron production cross section around the Z^0 resonance from LEP.	7
60	2.3 The Standard Model	9
61	2.4 Charge and Neutral Current Interactions	12
62	2.5 This plot shows the appearance and disappearance curves for a 2-flavor ap-	
63	proximation as a function of baseline. The values of $\Delta m^2 = 0.0025 \text{ eV}^2$	
64	and $\sin^2 \theta = 0.14$ are used.	14
65	2.6 Neutrino Mass Hierarchy	16
66	3.1 Diagram of a Time Projection Chamber	19
67	3.2 MicroBooNE TPC	21
68	3.3 MicroBooNE wires measured linear mass density	22
69	3.4 Tensioning system	23
70	3.5 Multiple wire planes installed in MicroBooNE	24
71	3.6 MicroBooNE tension measuring device	25
72	3.7 MicroBooNE tension map	26
73	3.8 MicroBooNE tension histogram	26
74	3.9 PMT optical unit	27
75	3.10 PMT optical unit	28
76	3.11 Detector Electronic layout	29
77	4.1 The Booster Neutrino Campus	30
78	4.2 BNB Target	32

79	4.3	Booster Neutrino Beamline	33
80	4.4	BNB Target	34
81	5.1	LSND Excess	36
82	5.2	MiniBooNE Event topology	38
83	5.3	MiniBooNE excess for ν and $\bar{\nu}$	39
84	5.4	Neutrino induces single π^0 production	40
85	6.1	Icarus Cosmic π^0	43
86	6.2	Wire Cell reconstruction of CORSIKA MC viewed in the BEE viewer	46
87	6.3	Photon distribution from π^0 s	49
88	6.4	Reconstructed energy sum and energy product for shower pairs. Both, the reconstructed energy sum and product is less than the true energy deposited.	50
90	6.5	Reconstructed vs. True opening angle	51
91	6.6	Single particle π^0 mass distribution	52
92	6.7	Single particle π^0 reconstruction efficiency	53
93	6.8	Cosmic π^0 production by parent process	54
94	6.9	Spatial decay points for cosmic π^0 s in MicroBooNE	55
95	7.1	Enhanced Signal Sample	58
96	7.2	Background Sample	59
97	7.3	Area normalized Data-Monte Carlo mass distributions	60
98	7.4	Direct data Monte Carlo rate comparison	61
99	7.5	Direct data Monte Carlo rate comparison	61

¹⁰⁰ List of Tables

¹⁰¹	4.1 Beam Production Systematics	34
¹⁰²	7.1 CORSIKA MC rates	57

¹⁰³ Chapter 1

¹⁰⁴ Introduction

¹⁰⁵ This thesis describes work towards electromagnetic shower reconstruction and steps towards
¹⁰⁶ a neutral current single π^0 cross section measurement motivated from reconstruction tech-
¹⁰⁷ niques used for neutron induced cosmogenic π^0 analysis. This thesis will use data from
¹⁰⁸ the MicroBooNE Liquid Argon Time Projection Chamber (LArTPC) located at the Fermi
¹⁰⁹ National Accelerator in Batavia, IL.

¹¹⁰

¹¹¹ To begin, Chapter 2 will provide some background about the neutrino. We will begin by
¹¹² presenting the initial premise for the need of a neutrino-like particle. Then, we will describe
¹¹³ the theoretical framework used to address how they interact the standard model. Finally we
¹¹⁴ will present the phenomenon known as neutrino oscillation and provide some mathematical
¹¹⁵ framework to describe it. Chapter 3 begins with a brief history of the LArTPC detector
¹¹⁶ technology and its use as a high precision neutrino detector. The chapter continues to
¹¹⁷ explain in depth the various subsystems that constitute the MicroBooNE detector. Chapter
¹¹⁸ 4 will describe how a neutrino beam is produced and delivered to the MicroBooNE detector.
¹¹⁹ It will focus on Fermilab's Booster Neutrino Beam (BNB) which generates a beam of nearly
¹²⁰ pure ν_μ or $\bar{\nu}_\mu$ around 1 GeV in average energy. Chapter 5 will present in detail the claims
¹²¹ of the electromagnetic ν_e -like excess first seen by the LSND experiment and then later
¹²² verified by the MiniBooNE experiment. This chapter will also discuss the neutral current
¹²³ cross section, which is the main background in the MiniBooNE excess claim. Chapter
¹²⁴ 6 will introduce MicroBooNE's cosmogenic background and motivate the importance of

understanding the cosmic rate. Here, we will also discuss the motivation to use cosmic π^0 events as a means of calibrating the detector energy scale. The cosmic backgrounds are addressed for the oscillation analysis and a future neutral current single π^0 measurement. Next, this chapter will address simulation, reconstruction, and event selection. Chapter 7 will present results from MicroBooNE cosmics data addressing the cosmic π^0 rate from neutral induced events. We will finish with conclusions from both the measurement and also comments on a new technique towards EM reconstructed showers.

Chapter 2

Neutrinos & Neutrino Oscillations

2.1 The History the Neutrino

The story of the neutrino began in Paris on a cloudy winter day in the year 1896. Parisian native, Henri Becquerel was experimenting with uranium salts and investigating the newly discovered x-ray radiation. [1] He hypothesized that when the salts were energized by sunlight they would produce the x-ray radiation. This hypothesis was disproven on the cloudy February 27th day when his experiment still detected radiation emitting from the salts in the absence of the sun. Becquerel had discovered radioactivity. In the coming years, this phenomena was supported by the work of Marie and Pierre Curie in studying the radioactivity of the element Thorium which lead to their discovery of the elements Polonium and Radium. These discoveries would later win Becquerel and the Curie's the 1903 Nobel Prize in Physics.

After radioactivity became an accepted phenomena in the science community, Ernst Rutherford discovered that radioactive decay products came in two different forms. He labeled them as α -decay and β -decay. At the time, beta decay was believed to be a two body decay where a nucleus A decays into a lighter nucleus A' and a β -particle(electron). The outgoing energy of the electron from a two body decay is given by equation 2.1. Assuming conservation of energy, the value of the outgoing energy should be discrete.

$$E_e = \frac{m_A^2 + me^2 - m_{A'}^2}{2m_A} \quad (2.1)$$

152 In 1914, James Chadwick had discovered that the energy spectrum of the β -particles
 153 were continuous as opposed to mono-energetic. While some scientist were willing to abandon
 154 the requirement of energy conservation, others found this to be an unpalatable solution.
 155 Unable to attend the 1930 Tubingen physics conference in Germany, Wolfgang Pauli wrote
 156 a letter to the attendees in which he proposed the first idea of the neutrino. An excerpt
 157 from his famous December 4th letter is translated from German below [2].

158 I have hit upon a desperate remedy to save the “exchange theorem” of statistics
 159 and the law of conservation of energy. Namely, the possibility that there could
 160 exist in the nuclei electrically neutral particles, that I wish to call neutrons,
 161 which have spin 1/2 and obey the exclusion principle and which further differ
 162 from light quanta in that they do not travel with the velocity of light. The
 163 mass of the neutrons should be of the same order of magnitude as the electron
 164 mass and in any event not larger than 0.01 proton masses. The continuous beta
 165 spectrum would then become understandable by the assumption that in beta
 166 decay a neutron is emitted in addition to the electron such that the sum of the
 167 energies of the neutron and the electron is constant...

168 In 1932, Chadwick discovered the neutron we know of today. Unfortunately, this neutron
 169 was too heavy to be the particle that Pauli had proposed. Expanding on Pauli’s work, Enrico
 170 Fermi proposed a more complete picture of beta decay and renamed Pauli’s ‘neutron’ to
 171 what is commonly called a *neutrino*. Fermi’s theory directly coupled the neutron with a
 172 final state proton, electron, and neutrino. This theory of beta decay, $n \rightarrow p + e^- + \bar{\nu}_e$
 173 preserves the law of conservation of energy and would later prove to be a more accurate
 174 description of the process.

¹⁷⁵ **2.2 Discovery of the Neutrino**

¹⁷⁶ Measuring and detecting neutrinos is a tricky business. In the 1950s, Clyde Cowan and
¹⁷⁷ Frederick Reines set out to directly measure neutrino interactions for the first time. If a
¹⁷⁸ free neutrino existed, they hypothesized that they could detect the byproducts from the
¹⁷⁹ inverse beta decay $\bar{\nu}_e + p \rightarrow e^+ + n$. They realized that such a measurement would require a
¹⁸⁰ very intense neutrino source and a large detector. Their first proposal, which was approved,
¹⁸¹ was to detonate a nuclear bomb to supply the large, instantaneous source of neutrinos. A
¹⁸² large detector filled with liquid scintillator would free fall down a mine shaft recording flashes
¹⁸³ of light from the ionizing positrons before landing on a bed of feathers and foam rubber.
¹⁸⁴ The original experimental schematic is shown in Figure 2.1. At that time, the theorized
¹⁸⁵ neutrino cross section was $10^{-43} \text{ cm}^2/\text{proton}$ while the existing measured limit was still 7
¹⁸⁶ orders of magnitude short in sensitivity. The bomb experiment would have worked but
¹⁸⁷ could not provide the level of sensitivity required to confirm detection for neutrino cross
¹⁸⁸ sections below $10^{-39} \text{ cm}^2/\text{proton}$. This was due to background interactions that came in
¹⁸⁹ time directly from the bomb.

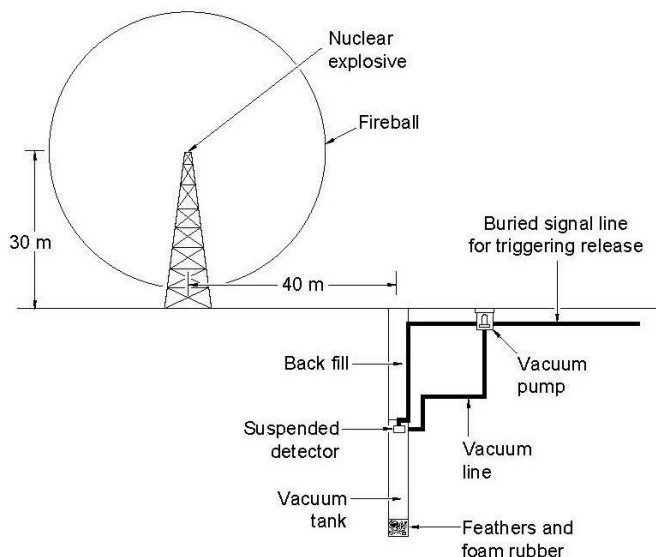
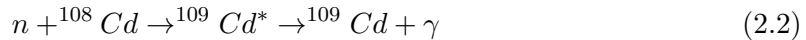


Figure 2.1: Original sketch of Cowan and Reines first proposed neutrino experiment.

Later, Reines realized tagging both the positron and neutron through a double coincidence would drastically reduce the backgrounds. This meant they could use a less intense neutrino source such as a nuclear reactor. They chose the Savannah River Plant near Augusta, Georgia which was estimated to produce neutrino fluxes on the order of $10^{12} - 10^{13}$ neutrinos/s/cm². The detector was composed of a water target that was doped with CdCl₂. As stated prior, the signal would rely on a double coincidence flash measured from photomultiplier tubes inside their detector. First, they would detect the positron as it annihilates with an electron via pair production ($e^+ + e^- \rightarrow \gamma + \gamma$). This is identified by two, back-to-back, coincident 0.511 MeV photons. Then, approximately 5 μ s later, a secondary photon would be detected which was produced from the neutron capture on Cadmium as shown in equation 2.2.



In 1956, only 25 years after Pauli's initial proposal of the neutrino, Cowan and Reines succeeded and provided the first direct experimental evidence of the electron flavor neutrino. In the subsequent years, the existence of two other flavors of neutrinos have been verified. In 1962, Lederman, Schwartz, and Steinberger discovered the ν_μ at Brookhaven National Laboratory by measuring neutrinos coming from pion decay. The ν_μ would be distinctly different from that of ν_e if the process $\nu_\mu + n \rightarrow p + e^-$ was forbidden. The results showed that the neutrinos from pion decay were indeed muon-like. Finally in 2000, the DONUT (Direct Observation of NeUtrino Tau) experiment stationed at Fermilab, made the first observed measurement of the ν_τ .

In 1956, C.S. Wu had shown that outgoing electron from beta decay maintained an opposing spin with respect to the spin of the parent nucleus. This turned out to be the first proof of maximal parity violation in weak interactions. Shortly thereafter, the neutrino helicity was first measured at Brookhaven National Labs by Maurice Goldhaber. In nature, neutrinos only have left handed helicity, while anti-neutrinos have right handed helicity. Helicity is frame dependent for particles with mass, which means there can be a reference frame in which the momentum vector can switch but the spin vector will not. For a

217 mass zero particles, this is not possible because the particle would already be traveling at
218 the speed of light. This assumption is what led to the belief that neutrinos were massless.

219 The number of active light neutrinos is well constrained by studying the decay of the
220 Z^0 boson at LEP (Large Electron-Positron collider). LEP was an electron-positron collider
221 ring with a circumference of approximately 27 km that supported four primary experiments
222 (L3, ALEPH, OPAL and DELPHI). The facility was coined the phrase “Z-Factory” due
223 to its ability to record approximately 1000 Z^0 boson decays every hour during optimal
224 running conditions. The number of active neutrinos, N_ν , is related to the width of the Z^0
225 resonance. Using 17 million Z^0 decays, LEP was able to show that $N_\nu = 2.9840 \pm 0.0082$

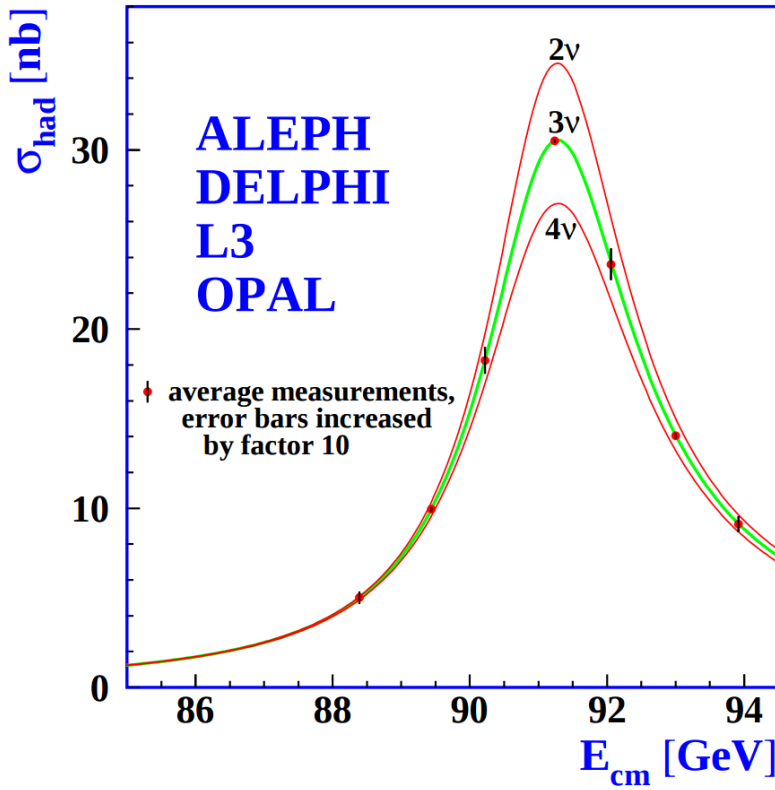


Figure 2.2: The Hadron production cross section around the Z^0 resonance from LEP. The curves for two, three, and four neutrino flavors are shown. The fit shows very compelling evidence of three active flavors of neutrinos.

226 2.3 Neutrinos in the Standard Model

227 In the later half of the 20th century, scientists were looking for a way to describe all the
228 fundamental forces and classify the known particles. The standard model of particle physics
229 is a phenomenological framework that describes the interaction of fundamental particles be-
230 tween the strong and electroweak forces. Having stood the test of time, the standard model
231 accurately predicts most elementary particle interactions, but, does have its limitations.
232 The standard model does not account for gravity nor does it account for many new physics
233 phenomena such as dark matter or dark energy. Most importantly, as we will see in section
234 2.5, it does not provide an accurate description of the neutrino.

235 The standard model consists of two types of particles, bosons and fermions. The funda-
236 mental bosons consist of two families: gauge bosons, which are typically the force carriers,
237 and scalar bosons, which refer to spin zero particles or fields. The gluon, photon, and the
238 weak boson are gauge bosons that mediate the strong, electromagnetic, and weak forces,
239 respectively. The Higgs boson is a scalar boson that possesses a nonzero vacuum expec-
240 tation value of 246 GeV. This provides a mechanism for certain particles to gain mass
241 even though their symmetries would suggest zero mass. The fundamental fermions are also
242 divided into two families, quarks and leptons each having three generations. The quarks
243 compose two main categories of particles, baryons and mesons. Baryons consist of an en-
244 semble of 3 quarks. The most common and stable baryons in the universe are protons (uud)
245 and neutrons (udd). Meson consist of an ensemble of quark anti-quark pairs and tend to
246 have shorter lifetimes than their corresponding baryons. The lightest and most common
247 mesons are pions ($u\bar{d}, d\bar{u}, u\bar{u}/d\bar{d}$) and kaons ($u\bar{s}, s\bar{u}, d\bar{s}/s\bar{d}$). The leptons are also divided
248 into two families with three generations each. The charged leptons, most notably the elec-
249 tron, interact via the electromagnetic and weak nuclear force and combine with nuclei to
250 form stable baryonic matter. The neutral leptons are the neutrinos and only interact via
251 the weak nuclear force. More details such as mass, charge, and spin for various particles
252 are shown in figure 2.3

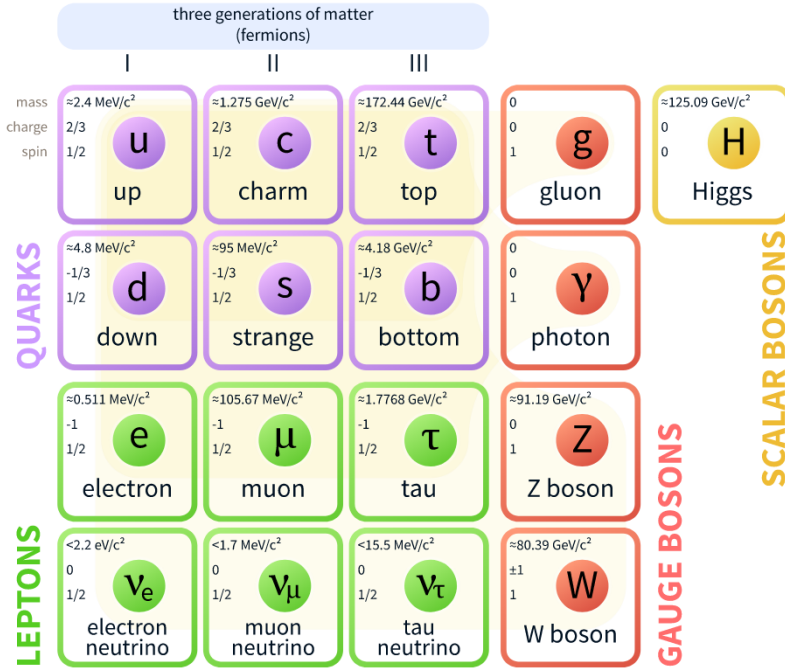


Figure 2.3: The current view of the standard model.

2.4 Neutrino Interactions

Neutrinos interact via the weak force. In the standard model, the weak force is unified with the electromagnetic force through an $SU(2) \otimes U(1)$ symmetry. The structure of the $SU(2)$ group symmetry accounts for the chirality of the fermion fields, along with ability to produce massive gauge bosons. The $U(1)$ group symmetry accounts for the massless photon propagator needed for electromagnetic interactions. For the quark and fermion families we define fermion fields in equations 2.3 and 2.4 , respectively. For formality we will define right(left)- handed neutrino(anti-neutrino) fields knowing that they will become irrelevant as the theory evolves:

$$\psi_1(x) = \begin{pmatrix} q \\ q' \end{pmatrix}_L , \quad \psi_2 = q_R , \quad \psi_3 = q'_R \quad (2.3)$$

$$\psi_1(x) = \begin{pmatrix} \nu \\ l \end{pmatrix}_L , \quad \psi_2 = \nu_R , \quad \psi_3 = l_R \quad (2.4)$$

262 We begin with the free Lagrangian, defined in equation 2.5, as it is already invariant in
263 flavor space.

$$\mathcal{L}_{\text{free}} \equiv \bar{\psi}(i\cancel{\partial} - m)\psi = i\bar{\psi}(x)\gamma^\mu\partial_\mu\psi(x) - m\bar{\psi}(x)\psi(x) \quad (2.5)$$

264 To make the Lagrangian invariant under local $SU(2) \otimes U(1)$, the fermion derivatives
265 have to be changed to covariant objects. This produces 4 different gauge parameters, shown
266 in equations 2.6, which correspond to the 4 different gauge fields required to describe the
267 W^\pm , Z^0 , and γ .

$$\begin{aligned} D_\mu\psi_1(x) &\equiv [\partial_\mu - ig\widetilde{W}_\mu(x) - ig'y_1B_\mu(x)]\psi_1(x) \\ D_\mu\psi_2(x) &\equiv [\partial_\mu - ig'y_2B_\mu(x)]\psi_2(x) \\ D_\mu\psi_3(x) &\equiv [\partial_\mu - ig'y_3B_\mu(x)]\psi_3(x) \end{aligned} \quad (2.6)$$

268 where, σ^i are the Pauli spin matrices and B_μ represents a field imposed by an external
269 source. We find that,

$$\begin{aligned} \widetilde{W}_\mu(x) &\equiv \frac{\sigma_i}{2} \left\{ \partial_\mu W_\nu^i - \partial_\nu^i + g\epsilon^{ijk}W_\mu^jW_\nu^k \right\} \\ B_{\mu\nu} &\equiv \partial_\mu B_\nu - \partial_\nu B_\mu \end{aligned} \quad (2.7)$$

270 The Lagrangian now satisfies $SU(2) \otimes U(1)$ symmetry between all gauge fields as shown
271 in equation 2.8. It should be noted that the fermion fields and gauge bosons are required to
272 be massless. This does not accurately describe the true interaction since 3 of the 4 gauge
273 bosons are known to have mass, but the theory does allow an interface between neutrino
274 interactions in the standard model.

$$\mathcal{L} = \sum_{j=0}^3 i\bar{\psi}_j(x)\gamma^\mu D_\mu\psi_j(x) \quad (2.8)$$

275 From equation 2.8, the terms that account for interaction of gauge bosons with the
276 fermion fields are shown below in equation 2.9

$$\mathcal{L} \rightarrow g\bar{\psi}_1(x)\gamma^\mu\widetilde{W}_\mu\psi_1(x) + g'B_\mu\sum_{j=0}^3 y_j\bar{\psi}_j(x)\gamma^\mu\psi_j(x) \quad (2.9)$$

277 From this, we are then able to construct the Lagrangian for both the charged and neutral
 278 currents. The charged current Lagrangian is shown in equation 2.10.

$$\mathcal{L}_{CC} = \frac{g}{2\sqrt{2}} \left\{ W_\mu^\dagger [\bar{q}\gamma^\mu(1-\gamma_5)q' + \bar{\nu}\gamma^\mu(1-\gamma_5)\bar{l}] + \dots \right\} \quad (2.10)$$

279 The neutral current term in the Lagrangian contains gauge fields for both the Z boson
 280 and photon, which can be broken into two terms to account for a non-zero Z boson mass
 281 while leaving the photon massless through spontaneous symmetry breaking (SSB). This is
 282 done through an arbitrary rotation, as shown in equation 2.11, where θ_w is known as the
 283 Weinberg or weak mixing angle. This angle is important because it is the angle used to
 284 rotate through SSB giving the Z boson its mass.

$$\begin{pmatrix} W_\mu^3 \\ B_\mu \end{pmatrix} = \begin{pmatrix} \cos\theta_w & \sin\theta_w \\ -\sin\theta_w & \cos\theta_w \end{pmatrix} \times \begin{pmatrix} Z_\mu \\ A_\mu \end{pmatrix} \quad (2.11)$$

285 It is then possible to write the neutral current Lagrangian that accounts for the inter-
 286 action of the Z boson as shown in equation 2.13.

$$\mathcal{L}_{NC} = \frac{e}{2\sin(\theta_w)\cos(\theta_w)} Z_\mu \sum_f \bar{f}\gamma^\mu(v_f - \alpha_f\gamma_5)f \quad (2.12)$$

287 where,

$$g\sin(\theta_w) = g'\cos(\theta_w) = e \quad \text{and} \quad \cos(\theta_w) = \frac{M_w}{M_z} \quad (2.13)$$

288 The neutral current coupling constants, v_f & α_f , differ with respect to the various
 289 quark, charged and neutral lepton fields. The neutrinos can be described as interactions via
 290 the charged and neutral currents. The Feynman diagrams, shown in figure 2.4, depict how
 291 the leptons couple to the quarks via the current mediator.

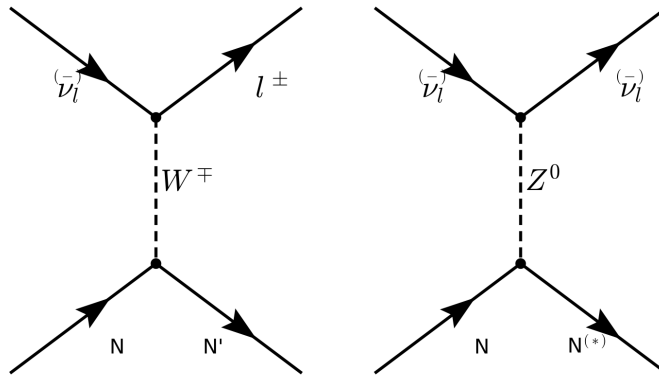


Figure 2.4: The Feynman diagram on the left describes a charged current (CC) neutrino interaction which transforms neutrinos into their corresponding charged leptons. In the CC interaction diagram the $N \rightarrow N'$ represents a changed nucleon charge. The diagram on the right shows the neutral current(NC) neutrino interaction with preserves the neutrino while it interacts. In the NC interaction diagram the $N \rightarrow N^*$ represents a same charge nucleon that could be at a higher resonance state.

2.5 Neutrino Mass and Flavor Oscillations

Neutrino oscillation is a quantum mechanical phenomenon in which the fraction of neutrino flavor changes while it propagates. This phenomena was first proposed in 1957 by Bruno Pontecorvo and relates the neutrino mass eigenstates with the flavor eigenstates through a rotation. This phenomena is best shown through a two neutrino flavor example, then extended into 3 flavors.

The mixing matrix for a two flavor neutrino case is:

$$\begin{pmatrix} \nu_e \\ \nu_\mu \end{pmatrix} = \begin{pmatrix} \cos \theta & \sin \theta \\ -\sin \theta & \cos \theta \end{pmatrix} \begin{pmatrix} \nu_1 \\ \nu_2 \end{pmatrix} \quad (2.14)$$

In this example, the flavor states are represented as ν_e and ν_μ which are expressed as a mixture of mass states ν_1 and ν_2 . For aesthetic reasons, we chose ν_μ to be part of the example because most man made neutrino beams produce a relative pure sample of ν_μ . The framework for this example is commonly used as an oscillation approximation and can be generalized to satisfy any case of two distinctly different flavor neutrinos.

304 Using the two flavor formalism a pure ν_μ neutrino state can be expressed as equation
 305 2.15

$$|\nu_\mu(0)\rangle = -\sin \theta |\nu_1(0)\rangle + \cos \theta |\nu_2(0)\rangle \quad (2.15)$$

306 The evolution of the state is governed by solving the time dependent Schröedinger
 307 equation for the initial muon state:

$$|\nu_\mu(t)\rangle = e^{-i\frac{Et}{\hbar}} |\psi(0)\rangle = -e^{-i\frac{E_1 t}{\hbar}} \sin \theta |\nu_1\rangle + e^{-i\frac{E_2 t}{\hbar}} \cos \theta |\nu_2\rangle \quad (2.16)$$

308 Assuming neutrinos travel near the speed of light, we rewrite equation 2.16 using the
 309 relativistic approximation, along with setting $c = \hbar = 1$ and $p_1 = p_2 = p$:

$$|\nu_\mu(t)\rangle \simeq -e^{-i(p_1 + \frac{m_1^2}{2p_1})t} \sin \theta |\nu_1\rangle + e^{-i(p_2 + \frac{m_2^2}{2p_2})t} \cos \theta |\nu_2\rangle \quad (2.17)$$

310 with,

$$E = \sqrt{p^2 + m^2} = p \sqrt{1 + \frac{m^2}{p^2}} \approx p + \frac{m^2}{2p} \quad (2.18)$$

311 Next, the mass terms are grouped together and defined as the absolute square difference,
 312 $\Delta m^2 \equiv |m_2^2 - m_1^2|$. We find that if the mass are different then the mass eigenstates propagate
 313 at different frequencies and give rise the oscillatory behavior. The time dependent state can
 314 now be wrote as:

$$|\nu_\mu(t)\rangle = e^{-i\phi} (-\sin \theta |\nu_1\rangle + e^{+i\frac{\Delta m^2}{2p}t} \cos \theta |\nu_2\rangle) \quad (2.19)$$

with, $e^{-i\phi} \equiv e^{-i\left(p + \frac{m_1}{2p}\right)t}$

315 To calculate the probability of the initial ν_μ state being measured as a ν_e state at some
 316 later time t , we need to calculate the absolute value squared of the overlap between the
 317 states. Utilizing the relationship $\langle \psi_i | \psi_j \rangle = \delta_{i,j}$, the overlap between the states is:

$$\langle \nu_e | \nu_\mu(t) \rangle = e^{-i\phi} (-\sin \theta \cos \theta + \sin \theta \cos \theta e^{i\frac{\Delta m^2}{2p}t}) \quad (2.20)$$

³¹⁸ The probability reduces to:

$$\begin{aligned}
 P(\nu_\mu \rightarrow \nu_e) &= |\langle \nu_e | \nu_\mu(t) \rangle|^2 \\
 &= e^{i\phi} e^{-i\phi} \sin^2 \theta \cos^2 \theta (-1 + e^{-i\frac{\Delta m^2}{p}t})(-1 + e^{+i\frac{\Delta m^2}{p}t}) \\
 &= \frac{1}{2} \sin^2 2\theta \left(1 - \cos \left(\frac{\Delta m^2}{2p} t \right) \right)
 \end{aligned} \tag{2.21}$$

³¹⁹ Finally, from relativistic assumptions, we set $p = E_\nu$ as the outgoing neutrino energy
³²⁰ and $t = L$ corresponds to the distance traveled.

$$P(\nu_\mu \rightarrow \nu_e) = \sin^2 2\theta \sin^2 \left(\frac{\Delta m^2 L}{4E_\nu} \right) \tag{2.22}$$

³²¹ From a proper accounting of numerical values of c and \hbar , equation 2.26 is more com-
³²² monly written as:

$$P(\nu_\mu \rightarrow \nu_e) = \sin^2 2\theta \sin^2 \left(1.27 \frac{\Delta m^2 L}{E_\nu} \right) \tag{2.23}$$

³²³ This oscillation behavior is best visualized as a plot of the probability of appearance
³²⁴ and disappearance as shown Figure 2.5.

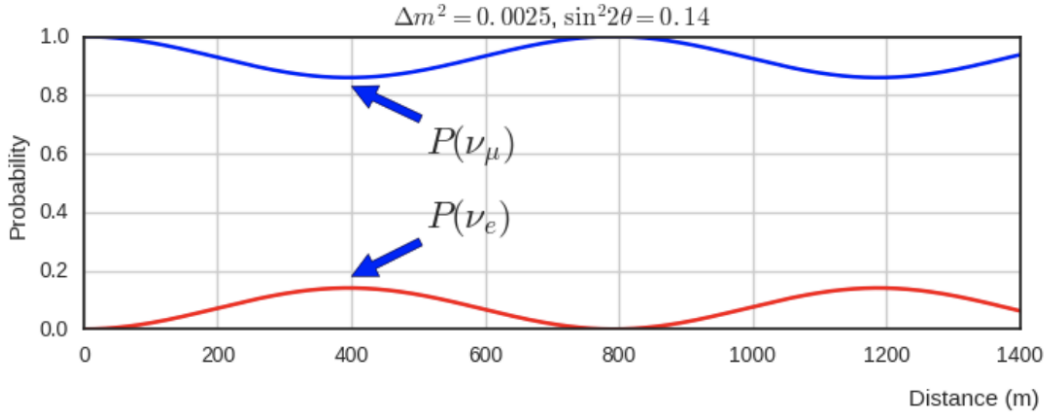


Figure 2.5: This plot shows the appearance and disappearance curves for a 2-flavor approximation as a function of baseline. The values of $\Delta m^2 = 0.0025 \text{ eV}^2$ and $\sin^2 \theta = 0.14$ are used.

325 As shown prior from figure 2.2, there are very good constraints on the number of active
 326 neutrinos[3]. Extending this formalism to a 3 flavor case was done by Pontecorvo-Maki-
 327 Nakagawa-Sakata (PMNS). The PMNS matrix is a 3 dimensional unitary matrix which
 328 is parameterized by three mixing angles $\theta_{12}, \theta_{23}, \theta_{13}$ a complex phase δ . The three angle
 329 correspond to the mixing effect, while δ is known as the charge parity (CP) phase. If the
 330 CP-phase is non-zero, then neutrinos violate charge parity conservation which leads to the
 331 conclusion that neutrinos and anti-neutrinos interact differently with matter. The value for
 332 δ has yet to be observed.

$$U_{PMNS} = \begin{pmatrix} 1 & 0 & 0 \\ 0 & c(\theta_{23}) & s(\theta_{23}) \\ 0 & -s(\theta_{23}) & c(\theta_{23}) \end{pmatrix} \begin{pmatrix} c(\theta_{13}) & 0 & s(\theta_{13})e^{-i\delta} \\ 0 & 1 & 0 \\ -s(\theta_{13})e^{i\delta} & 0 & c(\theta_{13}) \end{pmatrix} \begin{pmatrix} c(\theta_{12}) & s(\theta_{12}) & 0 \\ -s(\theta_{12}) & c(\theta_{12}) & 0 \\ 0 & 0 & 1 \end{pmatrix} \quad (2.24)$$

333 where $c(\theta_{ij}) \equiv \cos \theta_{ij}$ and $s(\theta_{ij}) \equiv \sin \theta_{ij}$. The matrix equation is now put into a more
 334 compact manor that relates the mixing of the 3 neutrino generations.

$$\begin{pmatrix} \nu_e \\ \nu_\mu \\ \nu_\tau \end{pmatrix} = \begin{pmatrix} U_{e,1} & U_{e,2} & U_{e,3} \\ U_{\mu,1} & U_{\mu,2} & U_{\mu,3} \\ U_{\tau,1} & U_{\tau,2} & U_{\tau,3} \end{pmatrix} \begin{pmatrix} \nu_1 \\ \nu_2 \\ \nu_3 \end{pmatrix} \quad (2.25)$$

335 In it's most general form, the oscillation probability is:

$$P(\nu_\alpha \rightarrow \nu_\beta) = \delta_{\alpha,\beta} - 4 \sum_{j>i} U_{\alpha,i} U_{\beta,i} U_{\alpha,j}^* U_{\beta,j}^* \sin^2 \left(1.27 \frac{\Delta m_{ij}^2 L}{E_\nu} \right) \quad (2.26)$$

336 From equation 2.26, we see that the oscillation probability is depended on the mass
 337 difference between states. Currently, there are no successful direct measurements of any
 338 given neutrino mass state. Therefore, there is an allowed ambiguity in the mass ordering
 339 of all three neutrino states. This is called the neutrino hierarchy problem. However, we do
 340 know that the difference between m_1 and m_2 is small relative to m_3 . Using this, we can
 341 build a picture of the fraction of different flavor eigenstates corresponding to their various
 342 mass states for both types of hierarchy.

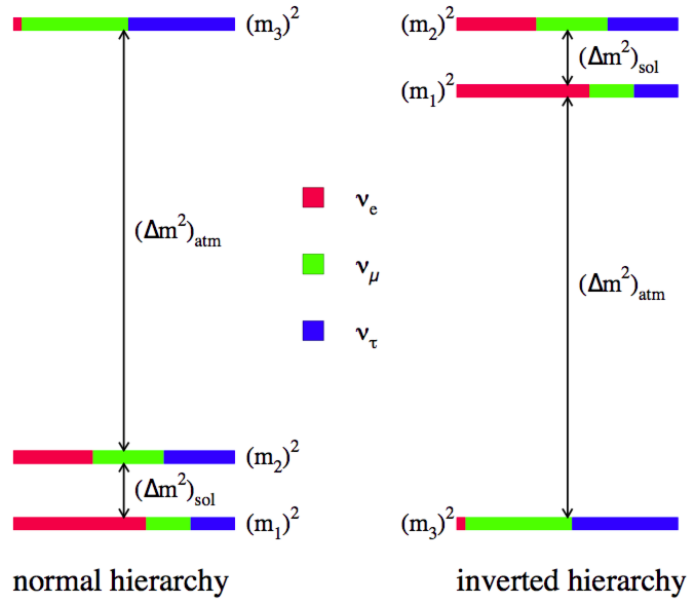


Figure 2.6: The two possible ordering for the 3 active neutrino mass eigenstates.

Many experiments have measured various elements of the PMNS matrix with neutrinos coming from accelerators, reactors, and solar sources. Currently, normal hierarchy ($m_1 < m_2 < m_3$) is favored. Therefore, we will show (table 2.27) the current Particle Data Group (PDG)[4] best fit values for oscillation parameters with respect to normal hierarchy.

$$\begin{aligned}
\Delta m_{21}^2 &= 7.37 \times 10^{-5} eV^2 \\
\Delta m_{32}^2 &= 2.50 \times 10^{-3} eV^2 \\
\sin(\theta_{12}) &= 0.297 \\
\sin(\theta_{23}) &= 0.437 \\
\sin(\theta_{13}) &= 0.0214 \\
\delta/4 &= 1.35
\end{aligned} \tag{2.27}$$

³⁴⁷ 2.6 Sterile Neutrinos

³⁴⁸ It is well accepted, from measurements at LEP[5], that there are only 3 neutrinos that couple
³⁴⁹ through the weak interaction. Mathematically, nothing prohibits a theory that allows for
³⁵⁰ neutrino mixing with other neutrino states beyond the 3 active states. These states, since
³⁵¹ they do not interact weakly, are called 'sterile neutrinos'. Extending the 3 flavor oscillation
³⁵² model to include any number of sterile neutrinos may be a possibility to address some the
³⁵³ currently unexplained results in the neutrino physics fields. Each additional state requires
³⁵⁴ an extra dimension to be added to the PMNS matrix. The sterile eigenstates are then
³⁵⁵ defined as

$$|\nu_{s_i}\rangle = \sum_j^{3+N} U_{s_i,j} |\nu_j\rangle \quad (2.28)$$

³⁵⁶ where N is the number of sterile neutrinos. The necessity for additional sterile neutrinos
³⁵⁷ was prompted by the LSND experiment and later supported by the MiniBooNE. experiment.
³⁵⁸ Both experiments are explained in depth in chapter 5. Each experiment found an excess
³⁵⁹ of electron-like events at low energy. This suggested a Δm^2 parameter space observed to
³⁶⁰ be 1eV^2 larger than expected and strongly contradicted the results of many other results
³⁶¹ which had Δm^2 around $\mathcal{O}(10^{-3}\text{eV}^2)$ and $\mathcal{O}(10^{-5}\text{eV}^2)$. This precipitated the need for
³⁶² further exploration of the LSND and MiniBooNE claims with more sophisticated detector
³⁶³ technologies. The MicroBooNE experiment was proposed in 2001 and will be the focal point
³⁶⁴ for this thesis.

365 Chapter 3

366 The MicroBooNE Detector

367 3.1 Brief History of LAr-TPC's

368 The surprising nature of neutrinos quickly prompted the need for precision measurements
369 of their interactions. Unfortunately, the low neutrino cross section posed a hurdle to build a
370 high statistics detector. In 1977, C.Rubbia propose a Liquid Argon Time Projection Cham-
371 ber (LArTPC) as large, high precision neutrino detector.[6] In 2001, The ICARUS collabo-
372 ration commissioned the T600 detector which was one of the first large scale LArTPC's to
373 be used as a neutrino detector. [7] The T600, which is comprised of 760 tons of liquid argon
374 was commissioned in Pavia, Italy using cosmic rays as a proof of principle. Later the T600
375 was place underground in Hall B of Laboratori Nazionali del Gran Sasso (LNGS) which is
376 located 730 km from the source of the CERN neutrino beam.

377 In 2009, the ArgoNeut collaboration, commissioned a small LArTPC in a 175 liter
378 vacuum jacketed cryostat. The ArgoNeut TPC was comprised of 3 wire planes and operated
379 at a drift field of 500 V/cm. The detector was placed just in front of the MINOS near
380 detector in the NuMI beam at Fermi National Accelerator Laboratory (FNAL)[8]. ArgoNeut
381 collected thousands of neutrino and antineutrino events providing valuable physics data and
382 detector R&D for future experiments with LArTPC's.

383 The MicroBooNE (the Micro Booster Neutrino Experiment) detector, which will be
384 discussed in depth throughout this chapter, is the first multi-ton LArTPC to be fully op-
385 erational in the U.S.[9] The MircoBooNE detector design pioneered many new detector

386 R&D concepts such as: the ability to maintain high LAr purity in an unevaluated vessel,
 387 implementation of low noise electronic readouts at liquid cryogenic temperatures and ad-
 388 vances in reconstruction techniques. MicroBooNE also supports a robust, high statistics
 389 physics program to address the MiniBooNE Low Energy Excess [10] and various cross sec-
 390 tion measurements. MicroBooNE was commissioned and began taking cosmic ray data in
 391 the summer of 2015. In October 2015 it began taking neutrino data. Shortly there after,
 392 the first neutrino event candidates were identified. [11]

393 3.2 Introduction

394 The MicroBooNE detector utilizes 170 tons of liquid argon to sustain 87 tons of active
 395 detector mass[12] It is located at the Liquid Argon Test Facility (LArTF) which is 470
 396 m downstream of the Booster Neutrino Beamline (BNB) source at the Fermilab National
 397 Accelerator Lab (FNAL) in Batavia, Illinois. The detector is the first large scale LArTPC
 398 to be deployed, commissioned and fully operated in the U.S.

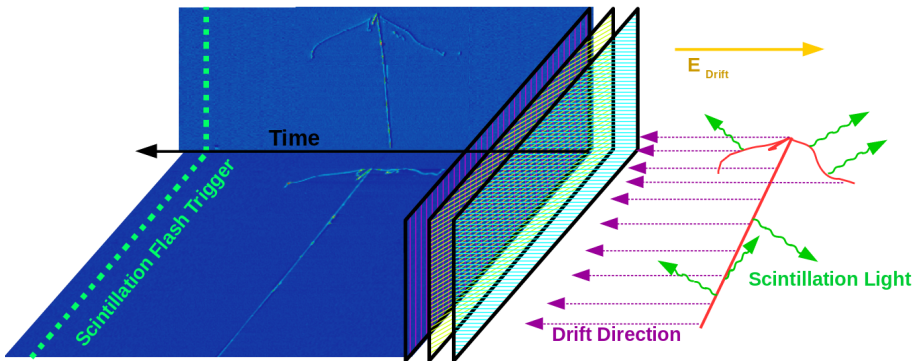


Figure 3.1: This diagram illustrates how a TPC works. First, charged tracks ionize the argon. The ions produce prompt scintillation light and the corresponding electrons begin to drift towards the wires due to the presence of the electric field. When the drift electrons reach the wire planes a 2D image is produced for each plane. When combining the 2D images from multiple planes along with the scintillation light information a 3D reconstruction is possible.

399 The general principle of a LArTPC involves utilizing two properties of LAr, scintillation

400 light and ionization. Charged particles travel through the argon and produce scintillation
401 light which is collected by photomultiplier tubes (PMT's). A uniform electric field is applied
402 over the active volume which transports the ionization electrons to a series of wire planes.
403 Assuming the argon is pure and has minimal electro-negative contaminants, the wire planes
404 then measure the induced or collected charge signal from the drifting electrons. The planes
405 are each oriented at a different pitch angles. Each plane can then produce a two-dimensional
406 image of the event as a function of wire and time. Combining multiple planes along with
407 the PMT information allows for the object to be fully reconstructed in three dimensions.
408 A diagram of the TPC concept is show in Figure 3.1. In the following sections the TPC,
409 light collection system, and electronics are described in detail.

410 **3.3 Time Projection Chamber**

411 The TPC is the core of the MicroBooNE detector and forms a rectangular prism with
412 dimensions $2.3\text{ m} \times 2.6\text{ m} \times 10.4\text{ m}$ which contains 87t of LAr. The longest dimension,
413 which in MicroBooNE's coordinate system is referred to as the z-direction, is oriented along
414 the axis of the BNB. The majority of the TPC materials are composed of 304V stainless
415 steel and G10. Stainless steel was chosen due to its low magnetic susceptibility, resistance
416 to corrosion/oxidation, and ability to maintain its strength in cryogenic temperatures. G10
417 was chosen due to it's ability to perform well as an insulator in cryogenic environments.



Figure 3.2: The MicroBooNE TPC is shown here. On the far right is the flat cathode plane. The far left shows the 8,456 anode wires installed. The field cage tubes, which provide the uniform electric field, span the length between the anode and cathode.

418 The TPC field cage, which provides the uniform electric field through the detector
 419 volume, and was designed to produce field strengths up to 500 V/cm in liquid argon. The
 420 field cage consists of a total of 64 stainless steel rectangular loops that are supported and
 421 evenly spaced by a G10 holder. The cathode plane is a series of flat stainless steel sheets
 422 that is opposite the anode sense wires. Figure 3.2 shows the MicroBooNE TPC.

423 Every piece that was used in the MicroBooNE detector was thoroughly cleaned. Many
 424 pieces were cleaned in an ultrasonic cleansing bath while others were cleaned by hand.
 425 The detector was constructed in a clean environment that maintained positive pressure to
 426 mitigate the accumulation of dust. A complete description of the process is summarize in
 427 a separate technical note. [13]

428 MicroBooNE has a total of 8,465 sense wires that form 3 unique wire planes, one vertical
 429 collection plane (Y) and two induction planes (U,V) oriented at $\pm 60^\circ$ relative the Y plane.
 430 The wire planes are separated by 3 mm. The wires in each plane are evenly spaced by 3
 431 mm pitch on carrier boards. The Y plane consists of 3,456 wires with a total of 108 carrier
 432 boards that accommodate 32 wires each. Each of the U and V planes consist of 2,400 wires
 433 with a total of 150 carrier boards that accommodate 16 wires each. The wires themselves
 434 are made of 304V stainless steel and are $150 \pm 5 \mu\text{m}$ in diameter. A $2\mu\text{m}$ layer of copper
 435 is plated over the wires to decrease the resistivity from $40 \Omega/\text{m}$ to $3 \Omega/\text{m}$. The reduced

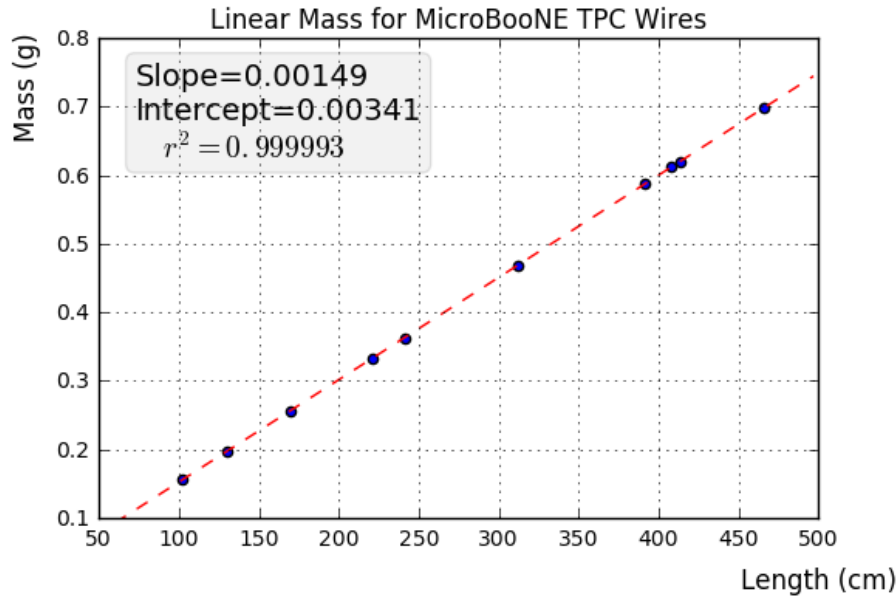


Figure 3.3: This plot is for a small sample used to cross check the linear mass density measured from the wire dealer. The slope from this plot represents the linear mass density and was found to be consistent with the value 0.149g/m . The linear mass density is important to properly account for the wire tension of each wire.

436 resistivity aids in noise reduction at cryogen temperatures. Finally the wire is covered in
 437 and outer layer $0.1\mu\text{m}$ of gold to prevent the copper from oxidizing over time. The linear
 438 mass density of a small sample of wires was measured and is shown in figure 3.3.

439 The wires were designed to installed at a nominal tension of 6.97 N . To account for this,
 440 the carrier boards were installed onto a series of tensioning bars on the anode frame. These
 441 tensioning system, as shown in figure 3.4, allowed for fine tune adjustments to be made to
 442 separate sections of wires.

443 There are a total of 12 tensioning bars, 2 sets of 5 that traverse the entire top and bottom
 444 length of the anode frame, and 2 spanning the entire height of the upstream and downstream
 445 sections of the anode frame. Bronze jacking screws were used for final adjustments once
 446 all the wires were installed. Bronze was chosen since it has a similar thermal expansion
 447 coefficient to stainless steel and it is a softer metal which helps mitigate the risk of cold
 448 welding with stainless steel during the tensioning process.

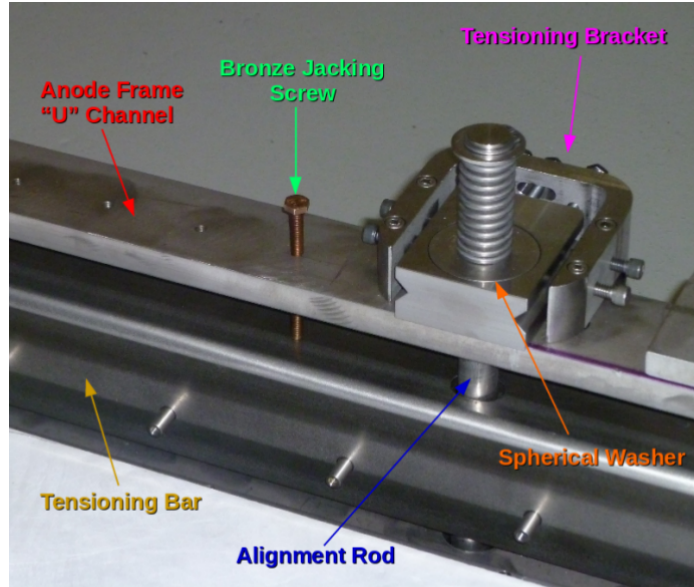


Figure 3.4: The MicroBooNE tension system. Wire carrier boards (not shown here) are mounted on the tensioning bar. The tensioning bar is able to move the wires during the tensioning process. Bronze jacking screws were used for final alignment during the tensioning process

449 In preparation for installing the actual detector wires, an installation team was trained
 450 on how to properly handle and install them. A 'mock-wire' installation was done to practice
 451 and identify the risks. After this, the actual wires were installed. The installation took
 452 approximately one week. The wires were installed serially, first the Y-plane, then the U-
 453 plane, and then the V-plane. After all the wires were installed, a G10 cover board was
 454 placed over carrier boards to secure and protect the electronics on the board, as shown in
 455 figure 3.5.

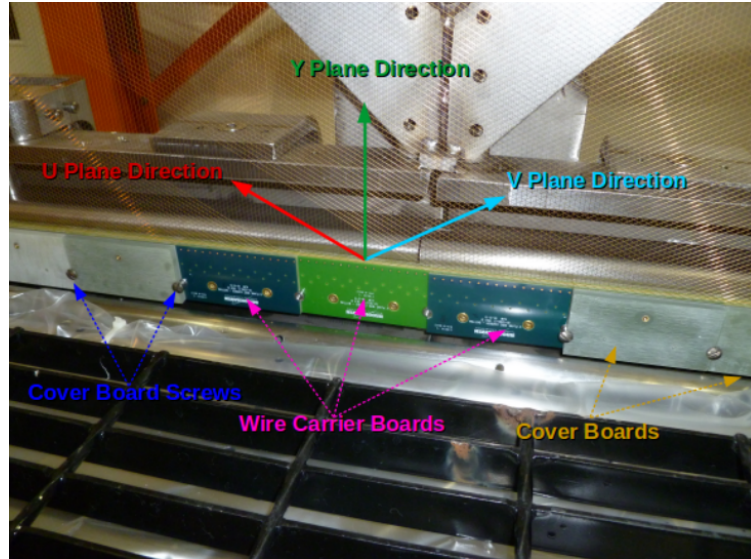


Figure 3.5: The MicroBooNE wires for 3 planes are shown here. The wire carrier boards are serially installed on the tensioning bar. The boards are held in place with a G10 cover plate that is secured with a smooth stainless steel screw.

456 Next, the wires were brought as close to nominal tension as possible. It was decided to
 457 favor under tensioning wires to minimize the risk of a broken wire during the tensioning
 458 process. The wire tensioning was done in a systematic way using the bronze jacking screws.

$$f = \frac{1}{2L} \sqrt{\frac{T}{\rho}} \quad (3.1)$$

459 Each wire has a characteristic resonance frequency that is related to its length, tension,
 460 and linear mass density through equation 3.1. A custom device was made to measure
 461 the resonant frequency of individual MicroBooNE wires. A laser light was focused on a
 462 particular wire and the wire gently plucked. A photo-diode mounted in an optical lens then
 463 measured the intensity of reflected light as the wire vibrated. The signals were then read into
 464 SpectrumAnalyzer, which is a software package that records frequency. SpectrumAnalyzer
 465 also allowed the high order frequency harmonics to be seen. The higher frequencies allowed
 466 for more precise tension measurement as see in Figure 3.6

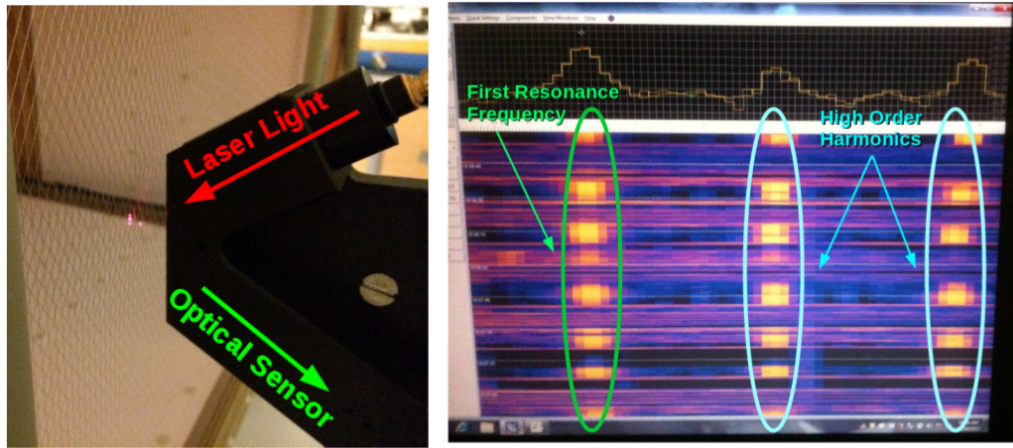


Figure 3.6: Left: Picture of the tension measuring apparatus including a laser and a optical sensor made of a photo-diode and a lens. Right: Example output of the SpectrumAnalyzer showing the first resonance frequency (bright line on the left) and the higher order harmonics (lines in the middle and left).

467 Note that the tension of 2328 out of 2400 U wires, 2308 out of 2400 V wires, and 3410
468 out of 3456 Y wires was measured, corresponding to 97.5 % of all wires installed in the
469 detector. Only the wires inaccessible to the tension measuring device were not measured.
470 The average tension for U,V,Y planes respectively was 0.589 ± 0.012 kg, 0.664 ± 0.014 kg,
471 0.525 ± 0.009 kg. The tension for each plane is shown in Figure 3.7 and Figure 3.8.

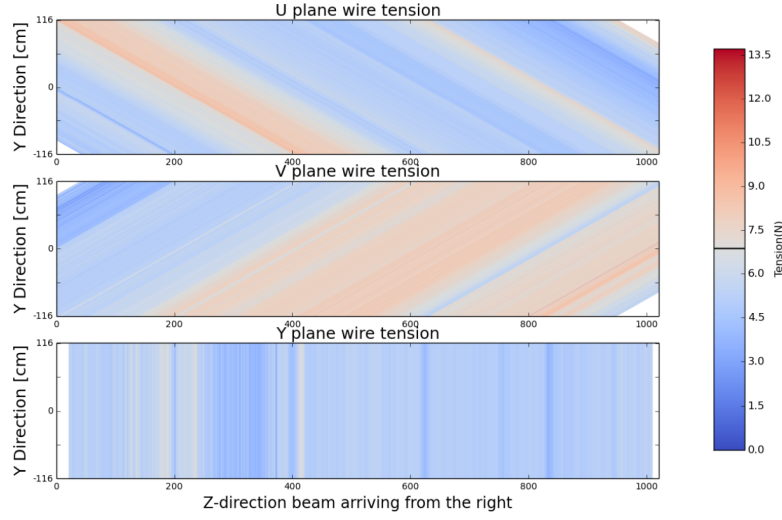


Figure 3.7: This a plane by plane map of the measured wire tensions for MicroBooNE.

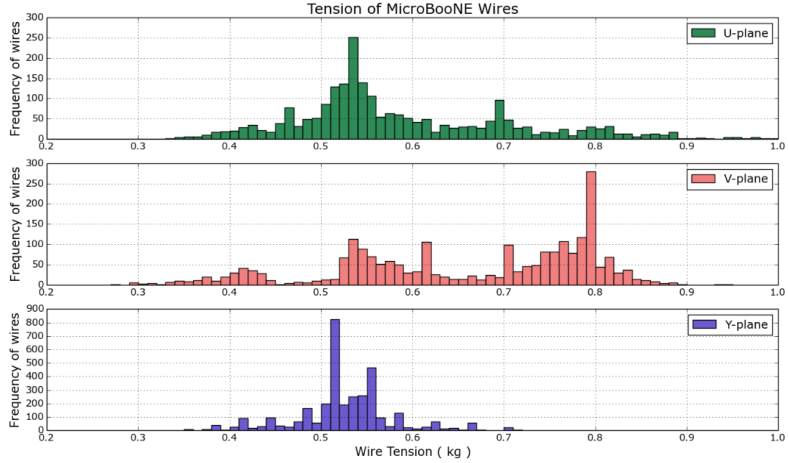


Figure 3.8: This a plane by plane histogram of the measured wire tensions for MicroBooNE.

472 3.4 Light Collection

473 The TPC can reconstruct 3D objects but there is still an ambiguity in the initial drift
 474 position. The light collection system in an LArTPC provides information to address this
 475 degeneracy. Scintillation light of liquid argon is 128nm wavelength and is produced through
 476 two primary reactions. The first, which accounts for $\approx 25\%$ of the light yield, is done
 477 through a Σ singlet excimer excitation and has a reaction time of 6 ± 2 ns. This type of

478 excimer is formed from an ionized argon atom that combines with another stable argon
 479 atom. The second, which accounts for the other 75% of light yield, is done through a Σ
 480 triplet excimer excitation and has a reaction time of $1590 \pm 100 \mu\text{s}$. The triplet state excimer
 481 is formed from a stable argon atom, an ionized argon atom, and a free electron. Since the
 482 prompt scintillation light is orders of magnitude faster than drift time from the TPC signal
 483 this information can be used to address this ambiguity.

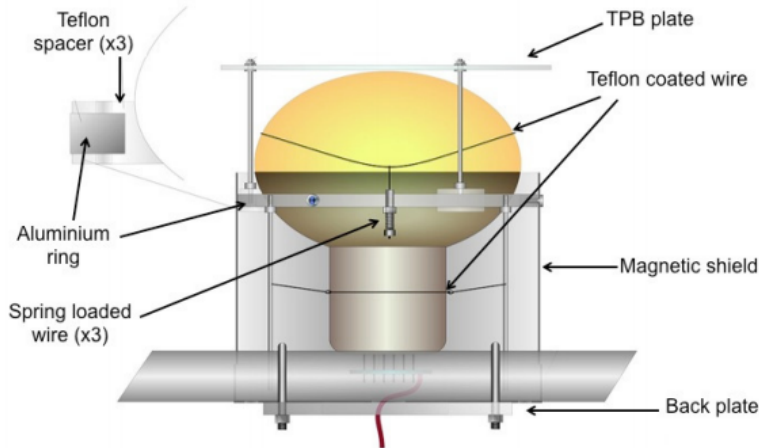


Figure 3.9: Schematic of a PMT optical unit for MicroBooNE.

484 The MicroBooNE light collection system consists of 32 8-inch diameter Hamamatsu
 485 R5912-02mod cryogenic PMTs. The PMT's are not optimized to detect 128nm light. There-
 486 fore, an acrylic plate coated with tetraphenyl butadiene (TPB)[14] was installed in front
 487 of the PMT's to act as a wavelength shifter. The TPB plate absorbs the 128nm light and
 488 re-emits at a peak wavelength of 425nm. Also, it is known that PMT response is reduced
 489 from certain orientations in the earth magnetic field. To address this a mu-metal shield was
 490 designed to extend just past the equator of the PMTs. A schematic of a PMT optical unit
 491 is shown in figure 3.9.

492 The PMT system is mounted on a railing behind the wire planes and spans the entire
 493 detector length as shown in figure 3.10. This also provides a weak handle on interaction
 494 position since the scintillation light is fairly localized. Most importantly, since MicroBooNE
 495 is a surface detector and constantly being bombarded by cosmic rays, the scintillation flash

496 is used as a method of identifying neutrino interactions coming in time with the beam.



Figure 3.10: PMT optical units installed on support racks inside the MicroBooNE cryostat

497 3.5 Electronics Readout

498 The TPC and PMT systems produce detector analog signals which need to be digitized,
499 transferred out of the detector, and written to disk through data acquisition (DAQ) software.
500 Both systems perform a first round of shaping and amplification in the cold LAr and then
501 interface with warm electronics for further processing. The DAQ continuously writes to disk
502 and creates a buffer which stores data for up to 24 hours. MicroBooNE employs various
503 triggers to signify beam and non-beam data blocks and permanently store data from the
504 buffer stream. A schematic overview of the TPC and PMT signal processing and readout
505 stages is shown in Figure 3.11.

506 For the TPC, a large portion of the electronics processing for the 8,256 wire signals
507 is performed directly in the LAr. To reduce electronics noise, the input distance from
508 the wires to the preamplifier is minimized. The sense wires directly interface with CMOS
509 analog front end ASICs which operate on cold motherboards. In total MicroBooNE has 516
510 CMOS ASICs. The ASICs generate 50 W of heat load which is a negligible impact on the
511 cryogenics system in order to prevent bubbles in the LAr. The motherboards shape and

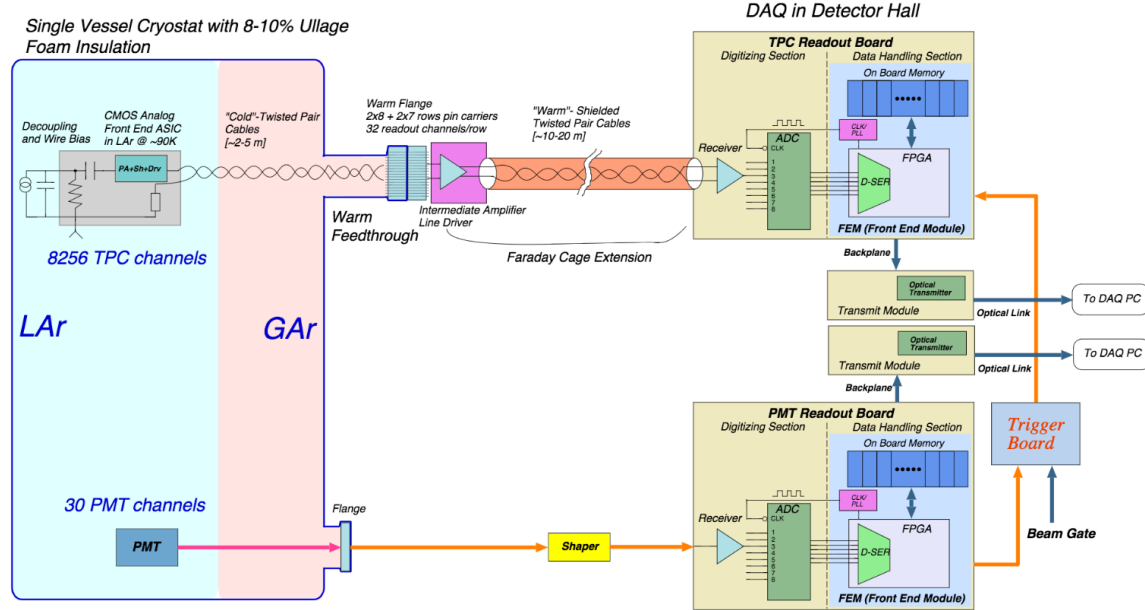


Figure 3.11: MicroBooNE LArTPC and PMT signal processing and readout schematic.

512 amplify the low noise signal. There are 36 top style motherboards that instrument Y, U
 513 and V plane wires and 14 side style motherboards that instrument U and V plane wires.
 514 The signals are then passed through a series of 12 feedthrough ports to warm electronics.
 515 The warm signals are then distributed over nine readout crates, which digitize the signals.

516 The TPC system read out frame is defined to be 1.6 ms. This number was chosen
 517 to account for ionization electrons that are generated at the cathode and drift the entire
 518 distance to the wires in the presence of a 500 V/cm E-Field. In MicroBooNE, an event
 519 is defined as four 1.6 ms readout frames. The additional frames allow for identification of
 520 cosmic particles that arrive before and after the neutrino interaction.

521 The PMT system is also processed in a similar fashion. The PMT's undergo 60 ns
 522 shaping to allow for precise measurements of the signal rising edge. The signals are sampled
 523 at 64MHz but only shaped signals above a threshold are read out and stored for data. The
 524 PMT signals are split into two different gains. A high gain signal that is 10 times the
 525 amplitude of the low gain. The signals are then brought to pre-amp/shaper boards and
 526 digitized and sent to the DAQ.

Chapter 4

Booster Neutrino Beam

Fermilab is one of the world's leading neutrino facilities and currently produces two neutrino beams that span a wide range of neutrino energies. The Booster Neutrino Beam (BNB), which will be described in detail throughout this chapter, is a lower energy beam that delivers neutrinos to various short baseline experiments. Fermilab also hosts the NuMI (Neutrinos at the Main Injector) Beam which produces neutrinos over a large range between 1 GeV/c - 30 GeV/c and delivers neutrinos to various experiments both on-axis and off-axis. The NuMI beam will not be covered in this thesis.

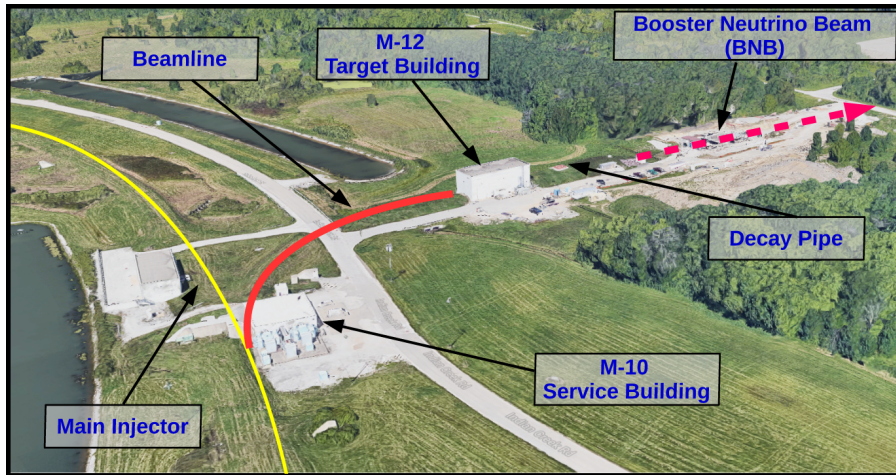


Figure 4.1: This image shows an aerial view of the Booster Neutrino Campus. Protons are extracted before the main injector near the M-10 service building and delivered to the M-12 target hall where the low energy neutrino beam is produced.

536 The Booster neutrino campus is illustrated in figure 4.1. To produce the BNB, pro-
537 tons are extracted from a transfer line just prior to the main injector and then interact
538 with a beryllium target. The following sections will describe the beam system, neutrinos
539 production process, and flux predictions for the BNB.

540 4.1 Primary Beam, Target and Horn

541 The BNB extracts 8.89 GeV/c momentum protons from the Fermilab Booster synchrotron
542 and delivers them to a Beryllium target housed in the M-12 building. The protons from
543 the booster are grouped in 1.6 μ s windows called 'beam spills'. One beam spill contains
544 approximately 5×10^{12} protons. On average the Booster can run no more than 5 Hz with
545 no more than 11 pulses in a row at 15 Hz. In optimal running conditions the Booster can
546 deliver 9×10^{16} protons on target (P.O.T) per hour.

547 The beam pipe directly leading to the target is approximately 5 feet long and is held
548 under vacuum to minimize proton interactions not originating from the target. The incom-
549 ing proton flux is measured by a pair of toroids which are positioned upstream of the target
550 and provide an error on P.O.T on the order of 2%.

551 The target consists of 7 cylindrical Beryllium slugs that together produce an effective
552 cylinder of 71.1 cm in length and 0.51 cm in radius. The use of multiple slugs gave the
553 Beryllium more surface area to allow efficient heat transfer from a simple air cooling system
554 to be sufficient. An exploded view of the BNB target is shown in figure 4.2. As the protons
555 collide with the beryllium, large amounts of secondary and tertiary mesons, such as π^\pm and
556 K^\pm , are produced. These mesons will later decay into neutrinos and other decay particles.

557 The target is positioned inside of a large toroidal electromagnet called a horn. The horn
558 is made of an aluminum alloy (6061 T6) and is pulsed with 174 kA of current to produces
559 a $1/R$ field where R is the distance from the axis of the horn. Since neutrinos are neutral
560 particles they cannot be directly focused by an electric or magnetic force. Instead, the horn
561 focuses the proper sign parent π^\pm, K^\pm in such a configuration that the neutrino angle from
562 the parent decay particles are focused in a beam.

563 Directly downstream of the horn/target assembly is a collimator that is used to reduced

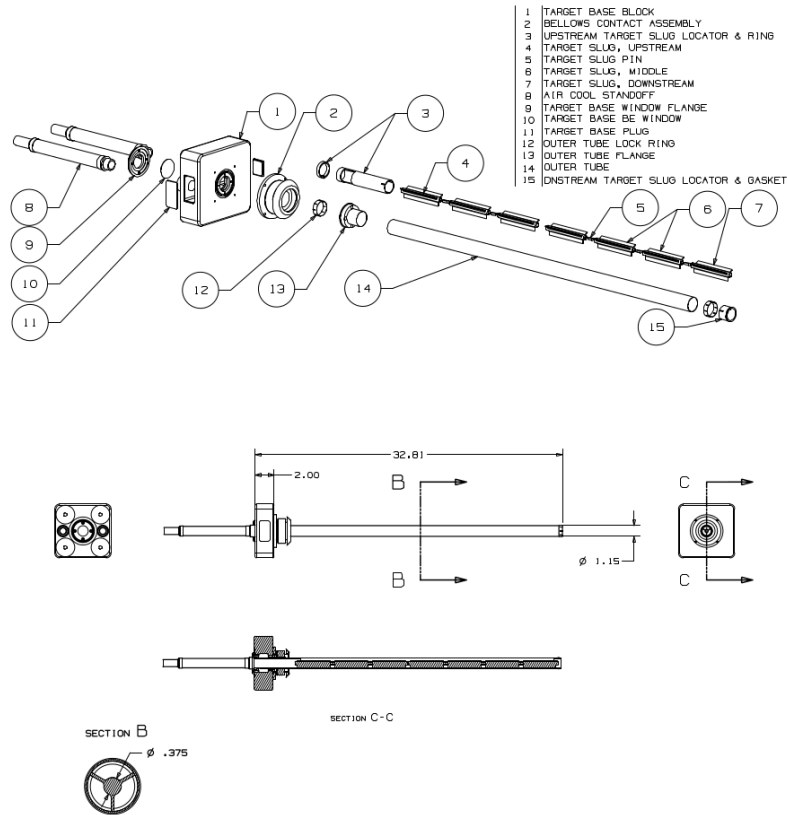


Figure 4.2: An exploded view of the BNB target which shows the 7 Beryllium slugs housed inside the support structure.

background coming from unwanted particles. Particles passing through the collimator enter a 45 m long decay region. In this region, most of the particles decay to produce the neutrino beam. At the end of the decay region there is a beam stop made of steel and concrete. There is also an array of gas proportional counters to detect high energy muons that punch through the beam stop. A diagram of the entire BNB system is shown in figure 4.3. When the horn polarity focuses (negative) positive charged mesons a (anti)neutrino beam is produced.

4.2 Neutrino Flux Prediction

The neutrino flux prediction for MicroBooNE uses the same GENIE simulation files used by MiniBooNE.[15] The files are feed into a Geant4 module that simulates the particles

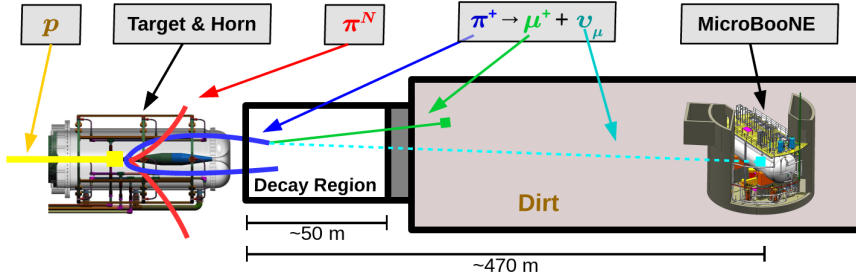


Figure 4.3: This figure shows the Booster Neutrino Beam line at FNAL. The neutrinos are produced in the decay region and then travel towards the MicroBooNE detector located 470 m down stream.

as they travel through the target, horn, and decay region. This produces a Monte Carlo (MC) flux estimate for each of the various neutrino types.[16] A systematics study was then performed to provide an error estimate for each of the ν_e , $\bar{\nu}_e$, ν_μ , and $\bar{\nu}_\mu$ flux predictions. To do this, 6 primary systematics were varied: the production rates of π^+ , π^- , K^+ , K^- , and K_L^0 , and a group systematic comprised of the horn current miscalibration, skin depth, nucleon inelastic, nucleon quasielastic(QE), nucleon total cross sections, pion inelastic, pion QE, and pion total cross sections. Beam errors for each of systematics are shown in Table 4.1 .The final flux estimate with the error uncertainty is shown in Figure 4.4.

	ν_μ	$\bar{\nu}_\mu$	ν_e	$\bar{\nu}_e$
Delivered P.O.T.	2.00%	2.00%	2.00%	2.00%
π^+	5.8%	0.46%	4.62%	2.66%
π^-	0.01%	7.51%	0.28%	3.20%
K^+	0.38%	0.13%	5.19%	2.61%
K^-	0.01%	0.35%	0.28%	3.92%
K_l^0	0.03%	0.27%	2.36%	22.59%
Other	5.78%	6.09%	3.6%	7.61%

Table 4.1: Systematic errors for production of various neutrino types with respect to their, P.O.T. , parent particle, and other variables.

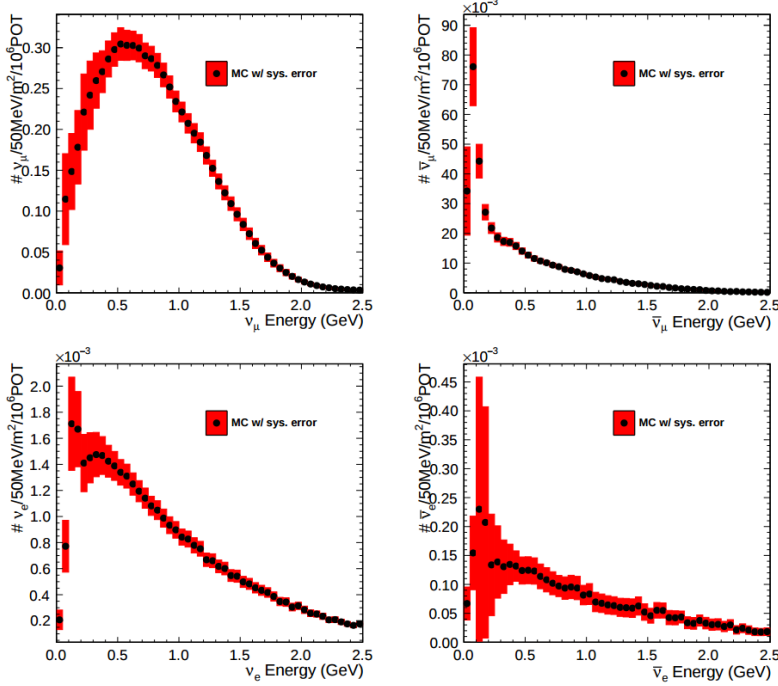


Figure 4.4: Monte Carlo flux predictions for the BNB neutrino spectrum. The red band represents the flux systematic errors. Note the orders of magnitude with the ν_μ spectrum rates.

581 Chapter 5

582 Low Energy Excess and Relevant 583 Cross Sections

584 5.1 Overview

585 This chapter will discuss various facets of what is commonly called the “MiniBooNE Low
 586 Energy Excess.” First, we will present the anti-neutrino excess observed by LSND and how
 587 the oscillation results can be interpreted. Then, we will discuss the efforts of MiniBooNE to
 588 understand the LSND results along with their oscillation results that establish the “Mini-
 589 BooNE Low Energy Excess.” We will also discuss the neutral current $1\pi^0$ cross section
 590 which is the dominant background in the oscillation analysis claims for both MiniBooNE
 591 and LSND. Finally, we will discuss MicroBooNE’s role towards addressing understanding
 592 the low energy excess claims of MiniBooNE.

593 5.2 LSND Excess

594 The Liquid Scintillator Neutrino Detector (LSND) was a 167 ton neutrino detector stationed
 595 at Los Alamos National Lab (LANL) designed to study neutrino oscillations. The detector,
 596 which hosted 1220 PMT’s for event detection, was placed 30 m away from the source of a
 597 low energy (40 MeV) $\bar{\nu}_\mu$ beam. Using the Los Alamos LAMPF beam, 800 MeV protons
 598 interacted with a water target to produce π^+ mesons which decayed into $\mu^+ + \nu_\mu$. The μ^+

599 would then interact with a copper beam stop and decay at rest to produce the low energy
 600 $\bar{\nu}_\mu$ beam.

601 The detector medium was primarily carbon (mineral oil CH_2). LSND could easily
 602 distinguish between electromagnetic showers (electrons/positrons/photon) or tracks (pi-
 603 ons/muons/protons) by differences in the Cherenkov cone that were produced. The oscil-
 604 lation signal interaction was $p + \bar{\nu}_e \rightarrow n + e^+$. The primary e^+ is easily visible from the
 605 Cherenkov light it produced but a neutron would not have produced Cherenkov light and
 606 therefore be invisible to the detector. The organic scintillator b-PDB was dissolved in the
 607 mineral oil at a concentration of 31 mg/l. The scintillator allowed the 2.2 MeV photon from
 608 the capture of the neutron on hydrogen to be detected. This allowed LSND a unique signal
 609 to identify $\bar{\nu}_e$ interactions. It should be noted that the detector technology could not easily
 610 discriminate between photons, electrons or positrons induced electromagnetic showers.

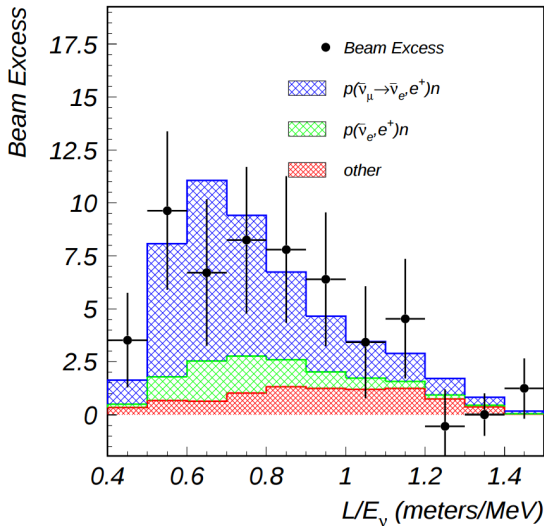


Figure 5.1: This is the LSND neutrino oscillation appearance plot as a function of L/E and represents the 87 event $\bar{\nu}_e$ excess claimed by the experiment.

611 In 2001, the collaboration published results for an observed excess of 87 ± 22.4 statistical
 612 , ± 6.0 *systm* events above the predicted background as shown in figure 5.1. If the excess is
 613 interpreted as neutrino oscillations from a two neutrino model, the best fit of the excess
 614 would suggest a $\sin^2(2\theta) = 0.003$ and $\Delta m^2 = 1.2 eV^2$ which greatly contradicts many other
 615 measurements for $\Delta m_{2,3}^2$ or $\Delta m_{1,3}^2$ [17]. One explanation for the excess suggests the idea of
 616 mixing between other additional neutrino states. These neutrinos are called ‘sterile’ since
 617 they cannot directly couple via weak interaction as mentioned prior from the constraints
 618 from LEP.

619 5.3 MiniBooNE Excess

620 The Mini Booster Neutrino Experiment (MiniBooNE) was designed to address the claims of
 621 the LSND $\bar{\nu}_e$ excess result. The MiniBooNE detector was a mineral oil Cherenkov detector
 622 designed to be a similar technology to LSND[18]. MiniBooNE, stationed at FNAL in the
 623 BNB, was positioned 541 m from the neutrino source and was able to receive both ν_μ and
 624 $\bar{\nu}_\mu$ fluxes. The distance was chosen such that the L/E parameter were similar to that of
 625 the LSND experiment.

626 MiniBooNE, which contained 818 tons of mineral oil (CH_4), was located underneath
 627 more than 3m of earth overburden to help reduce cosmic rays. The detector supported a 35
 628 cm thick outer cosmic veto using 240 PMT’s. The veto efficiency was 99.99% for rejecting
 629 cosmic muons. The inside of the detector was instrumented with 1,280 8-inch PMT’s
 630 which were used to read out neutrino and comsic data. Cherenkov light from different
 631 particles produced distinct patterns on various PMT’s inside the spherical detector. A
 632 cartoon showing various type of signal topologies from the MiniBooNE detector is shown
 633 in figure 5.2. The detector energy scale was calibrated *in situ* by fitting various parameters
 634 from through going muons, decay Michel electrons, and π^0 decays. A clear limitation of
 635 Cherenkov detectors is the inability to concretely distinguish between photon induced or
 636 electron induced showers.

637 The primary oscillation analysis for MiniBooNE was done ‘blind’ in an attempt to
 638 gain confidence from the physics community upon its findings[19]. The entire analysis was

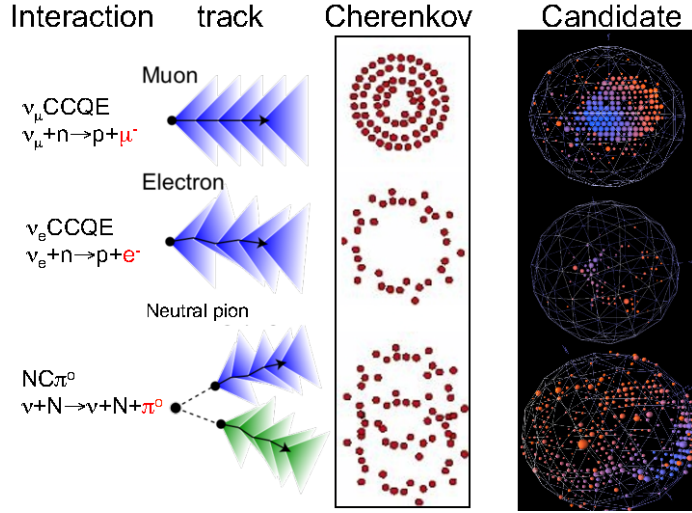


Figure 5.2: This cartoon depicts different particle interactions as observed in Cherenkov detector. The far right shows the interaction types as viewed in MiniBooNE

639 developed on large statistics Monte Carlo simulation and a small sample of test data. In
 640 total, MiniBooNE accumulated 6.46×10^{20} P.O.T. of ν -data and 11.27×10^{20} P.O.T. of
 641 $\bar{\nu}$ -data. Fermilab's ability to support both neutrino and anti-neutrino beams allow for
 642 MiniBooNE to confirm that an LSND-like excess was independent of neutrino type. The
 643 MiniBooNE data is in good agreement between signal and background predictions but
 644 contradicts the LSND claim up to 98% confidence in both modes above 500 MeV. The
 645 excess is most prominent in the region of events below 500 MeV, as seen in figure 5.3.
 646 In this region the largest background comes from π^0 -misidentification followed by photons
 647 coming from radiative Δ decays. MiniBooNE reports a total excess of 240.0 ± 62.9 combined,
 648 $(162.0 \pm 47.8\nu, 78.4 \pm 28.5\bar{\nu})$ events in the neutrino energy range $200 < E_\nu^{QE} < 1250\text{MeV}$.
 649 Also, if the excess is interpreted as a two flavor oscillation the inferred parameters are
 650 consistent with the LSND result.

651 5.4 Neutral Current π^0 production

652 The leading background from the MiniBooNE oscillation result, as mentioned in chapter 5.3,
 653 is π^0 -misidentification. Accurately measuring the neutrino induced neutral current single

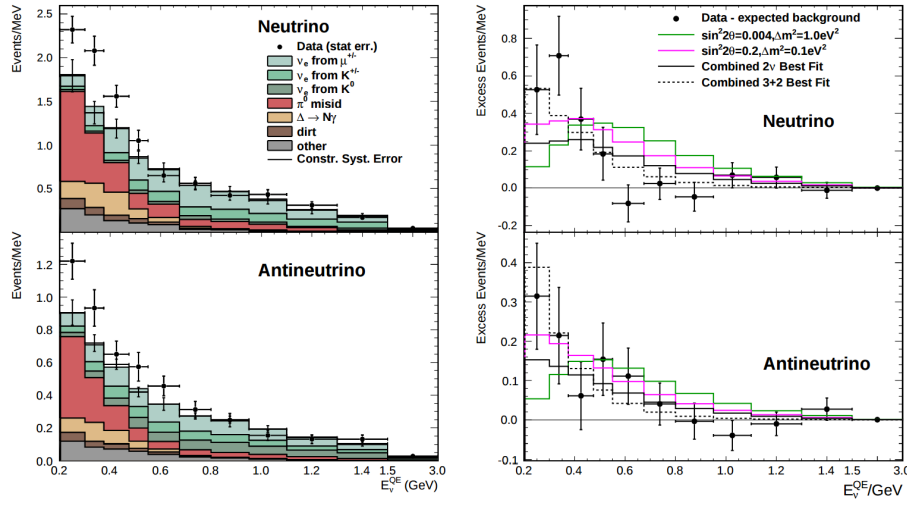


Figure 5.3: The left plots show the stacked histograms for signal and background overlaid with data for both neutrino and anti-neutrino modes. The right plots show the relative excess as a function of neutrino energy and make obvious the energy range that drives the excess.

π^0 production cross section is therefore crucial in understanding background contributions for an oscillation analysis. Charged current π^0 production conveniently has an outgoing charged muon in the final state and is very easy to identify. On the other hand, neutral current π^0 production does not guarantee any outgoing charged particles and therefore, makes identification much harder. For neutrinos in the BNB, the main production mode for neutrino induced neutral current π^0 production is via the $\Delta(1232)$ resonant production. Resonant production is when a baryon, such as a proton or neutron, is excited to a higher resonance state and then subsequently decays back to the initial state while liberating a π^0 . There are other neutrino induced π^0 production modes that MicroBooNE is sensitive to such as deep inelastic scattering and coherent production, but have a lower production cross section at the given BNB neutrino energy range. A general Feynman diagram can be used to describe the main components of neutrino induced neutral current single π^0 production in argon as seen in Figure 5.4.

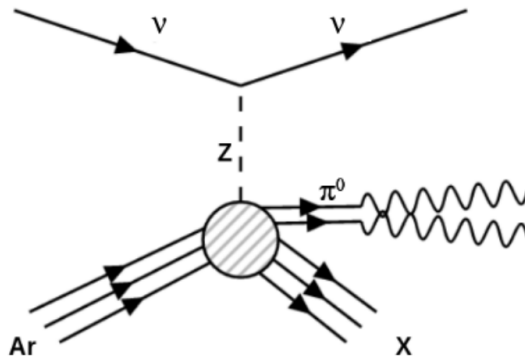


Figure 5.4: Neutrino induced single π^0 production on argon. This topology is defined such that single π^0 is produced and the other particles leaving the interaction (X) must only consist of nucleons.

667 5.5 NC- π^0 in Carbon vs Argon

668 In 2010, MiniBooNE measured the total neutral current single π^0 cross section on carbon
 669 with what is currently the world's largest statistics sample of π^0 s. The MiniBooNE neutral
 670 current single π^0 signal is defined as a topology that produces one and only 1 π^0 in the
 671 final state with no other other charged leptons or mesons originating from the vertex. In
 672 2015, the first measurement of neutrino induced neutral current π^0 production on argon was
 673 measured by ArgoNeut collaboration at Fermilab while running in the NuMI neutrino beam.
 674 AgroNeut, being a smaller detector, could not easily contain many of the electromagnetic
 675 showers from π^0 decays. This forced the analysis choose a slightly different final state signal
 676 definition requiring there to be at least one π^0 , no electron or muon, and allowing there
 677 to be any number of mesons in the final state. This modified signal definition makes any
 678 comparison to other historical data very complicated.

679 MicroBooNE, which resides in the same neutrino beam line as MiniBooNE, is a prime
 680 candidate for various studies of neutral current π^0 production studies between different
 681 target materials (C/Ar). Being a larger LArTPC, more π^0 decays will be contained allowing
 682 for high statistics measurements of the cross section along with the general need to measure
 683 the production rate as input to its own oscillation analysis.

684 Chapter 6

685 Cosmogenic π^0 s at MicroBooNE

686 In this chapter we will talk about some of the challenges and interesting physics cases re-
687 garding cosmogenics in a surface LArTPC. Many cosmic ray particles penetrate surface
688 detectors and populate the detector region making it necessary to remove these particles
689 from reconstruction and address charge contamination in neutrino events. The majority
690 of this chapter will emphasize cosmogenic track removal, electromagnetic showers and sub-
691 sequently π^0 selection. We will first examine some historical cosmogenic studies from the
692 Icarus experiment. Then, introduce what MicroBooNE can contribute in terms of un-
693 derstanding cosmics. We will address the cosmic simulation that is used, various steps in
694 reconstruction and pattern recognition used to select π^0 s in a LArTPC. Finally, we will con-
695 clude with how these studies impact future cross section analyses and backgrounds toward
696 the low energy excess analysis.

697 6.1 Motivation

698 Cosmogenic particles allow for the separate test of reconstruction tools along with an inde-
699 pendent way to address the detector energy scale. The high rate of surface cosmics cause
700 some trouble with disentangling signal neutrino events from cosmic ray removal. Luckily,
701 off beam surface cosmogenic samples allow for a large statistics dataset to develop and op-
702 timize reconstruction techniques. Cosmogenic muons that traverse the detector provide a
703 handle to understand detector energy scale along with understanding track reconstruction

efficiency. Stopping muons that produce a Michel electron help provide a benchmark for low energy showers in the 10's of MeV range. The π^0 resonance, with a mass of $134.9 \text{ MeV}/c^2$, can be used as a standard candle to benchmark overall detector energy scale. The calculated the π^0 mass, as shown in equation 6.1, depends on a measurement of energy and photon opening angle.

$$\mathcal{M} = \sqrt{2E_1E_2(1 - \cos\theta_{12})} \quad (6.1)$$

Electromagnetic shower reconstruction for LArTPC's is well known to be a hard task. The high resolution of the 2-dimensional projections of EM-showers introduce many challenges to develop unbiased and fully automated reconstruction. In 2001, the T600 ICARUS detector [20] performed a surface test run in Pavia, Italy. During this 100 day test the detector collected over 30,000 cosmic ray events. In 2008, the ICARUS collaboration published a study of electromagnetic showers coming from π^0 decays in the Pavia dataset. To select candidate π^0 events, ICARUS hand scanned a total of 7,500 potential events from a PMT triggered sample. Their hand scanning requirements included, that at least two well separated electromagnetic showers were visible, a valid t_0 time for the vertex, and that there was not much charge contamination coming from a nearby cosmic muon. After this, they were left with 212 hadronic interactions with at least one candidate neutral which they then proceeded to reconstruct. Their final reconstruction consisted of energy scaling to account for missing charge in the shower and a minimization against the true π^0 mass. An example of one of their hand scanned clustering events is shown in Figure 6.1.

MicroBooNE, being a surface detector, is in a position to do a similar study with improved reconstruction techniques. Also, understanding the cosmic production rate for single π^0 s is valuable to any MicroBooNE analysis that involves EM-showers. The following sections will present MicroBooNE's Monte Carlo simulation and state of the art reconstruction techniques.

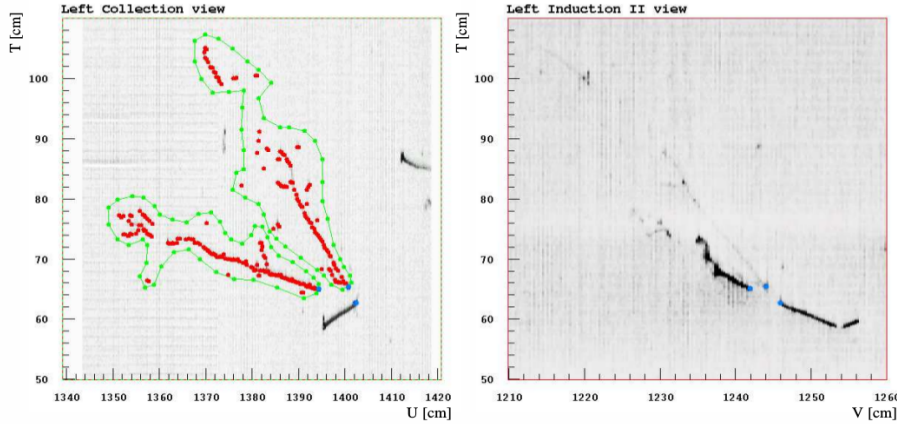


Figure 6.1: A cosmic π^0 from the ICARUS Pavia run. The left image shows the hand drawn clustering and positions of the shower conversion point and vertex point. The right image shows the same event on a different wire plane view.

6.2 Traditional Reconstruction

The traditional approach for LArTPC reconstruction involves grouping drift charges that are deposited on the wires to form wire-hits. The light collection system also has light-hits which corresponded to collected light of an individual track or shower. A group of PMT's that have light-hits at the same time is called a flash. Hits from each of the wire planes are clustered together with various reconstruction algorithms to form reconstruction objects that relate to individual particles in the detector. There are two primary reconstruction objects: tracks, which are mostly linear and compact clusters that represent muons, protons, and charged pions, and showers which are more fuzzy shaped cluster objects that represent photons and electrons. Next, to reconstruct a 3D object, an algorithm must match the same 2D cluster objects in at least two of the three wire planes. For MicroBooNE, and the general LArTPC community, matching track reconstruction is well advance but shower reconstruction suffers many pitfalls. In recent years lots of progress has been made for LArTPC shower reconstruction. Various different techniques such as improved 2D clustering and matching techniques, sophisticated pattern recognition tools[21], and deep learning[22] approaches have been explored and each has its various strengths and weaknesses.

744 6.3 Wire Cell Imaging

745 The traditional approach is not the only way to reconstruct LArTPC data. Instead, wire
 746 data can be treated with a tomographic approach directly producing a set of 3D space
 747 points. Although computationally intensive, this approach allows for more information to
 748 be used in a 3D clustering framework which can directly impact shower reconstruction and
 749 mitigate degeneracies from the 2D matching method.

750 The Wire-Cell framework, spearheaded by Brookhaven National Labs (BNL), utilizes
 751 this approach to create 3D space points from MicroBooNE's TPC data. The approach
 752 relies on the assumption that the same amount of ionization charge is seen on each plane.
 753 In MicroBooNE this is done by reconstructing small time slices on each wire planes. Each
 754 time slice involves solving a charge equation for all possible hits with respect to the matrix of
 755 hits actually recorded in the time slice. The charge equation is shown in equation 6.2. The
 756 detector wire signals are represented in matrix W while all potential wire hits are contained
 757 in H. Nonzero values in the Q matrix will correspond to unique wire-plane intersections of
 758 charge, near zero values represent ghost hits due to degeneracies in the charge equation.

$$\begin{bmatrix} W_{u_1} \\ \vdots \\ W_{u_n} \\ W_{v_1} \\ \vdots \\ W_{v_n} \\ W_{y_1} \\ \vdots \\ W_{y_n} \end{bmatrix} = \begin{bmatrix} Q_{u_1}^{H_1} & Q_{u_1}^{H_2} & \dots & \dots & \dots & Q_{u_1}^{H_{m-1}} & Q_{u_1}^{H_m} \\ \vdots & \vdots & \ddots & \ddots & \ddots & \vdots & \vdots \\ Q_{u_n}^{H_1} & Q_{u_n}^{H_2} & \dots & \dots & \dots & Q_{u_n}^{H_{m-1}} & Q_{u_n}^{H_m} \\ Q_{v_1}^{H_1} & Q_{v_1}^{H_2} & \dots & \dots & \dots & Q_{v_1}^{H_{m-1}} & Q_{v_1}^{H_m} \\ \vdots & \vdots & \ddots & \ddots & \ddots & \vdots & \vdots \\ Q_{v_n}^{H_1} & Q_{v_n}^{H_2} & \dots & \dots & \dots & Q_{v_n}^{H_{m-1}} & Q_{v_n}^{H_m} \\ Q_{y_1}^{H_1} & Q_{y_1}^{H_2} & \dots & \dots & \dots & Q_{y_1}^{H_{m-1}} & Q_{y_1}^{H_m} \\ \vdots & \vdots & \ddots & \ddots & \ddots & \vdots & \vdots \\ Q_{y_n}^{H_1} & Q_{y_n}^{H_2} & \dots & \dots & \dots & Q_{y_n}^{H_{m-1}} & Q_{y_n}^{H_m} \end{bmatrix} \begin{bmatrix} H_1 \\ H_2 \\ \vdots \\ H_{m-1} \\ H_m \end{bmatrix} \quad (6.2)$$

759 Then, each ‘slice’ is stacked to its corresponding x position. This produces a set of 3D
760 space points that can be used in pattern recognition algorithms to identify different particles
761 in the data. All reconstruction is done with accounting for known detector dead regions.
762 The current state of MicroBooNE’s signal and noise processing and imaging that requires
763 a minimum of 2 wire planes to be matched from the charge equation.

764 6.4 Pattern Recognition

765 Various pattern recognition tools are needed to address MicroBooNE’s TPC data but for
766 this analysis they can be generalized into two efforts, cosmic track removal and EM-shower
767 clustering. Being that the Wire Cell imaging technique is a new approach, an independent
768 analysis framework named Sp0ter was built. Sp0ter is written primarily in Python and
769 leverages many common packages. The framework is able to ingest 3D space points from
770 Wire Cell, clusters track and shower objects, and focuses on selecting and reconstruction
771 single π^0 events. First, we will focus on optimizing track removal. This involves identifying
772 tracks that are through-going, and contained. Once all the charge associated with tracks
773 are removed, the remaining charge is clustered into candidate EM-shower objects. Finally,
774 correlated shower pairs are identified and selected as candidate π^0 events.

775 A image of a typical MicroBooNE cosmic event reconstructed with 3D wire cell space
776 points are shown in Figure 6.2 using the BEE viewer [23]. A detailed list of reconstruction
777 and selection parameters are listed in the appendix.

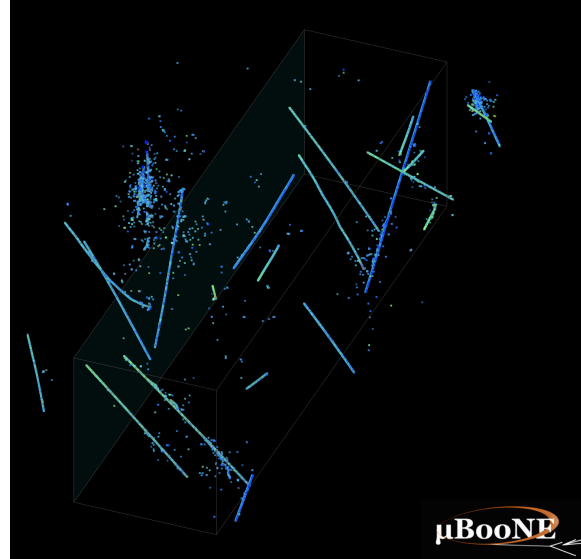
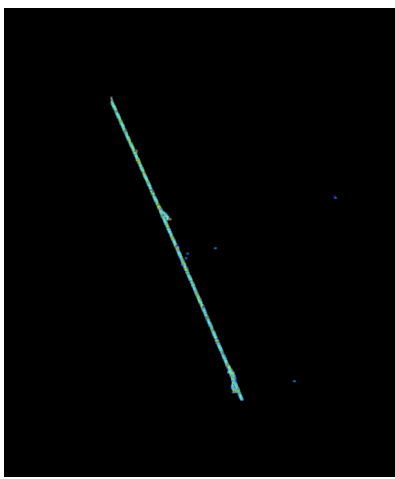


Figure 6.2: This is a typical cosmic event in the MicroBooNE detector. The data used to generate this event is CORSIKA Monte Carlo.

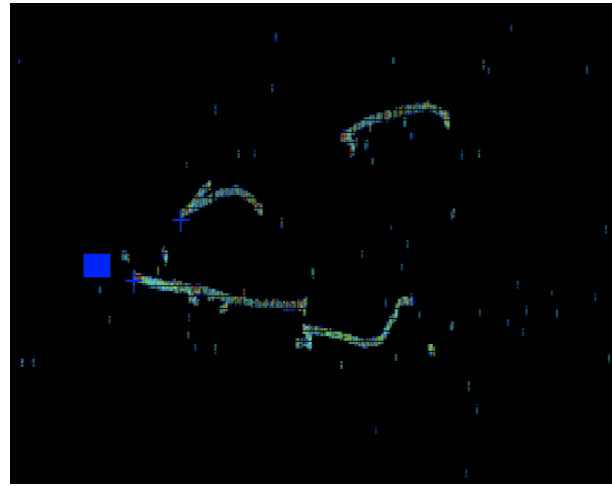
778 6.5 Clustering

779 The wire cell data produces a set of 3D space points as mentioned in section 6.3. Only space
 780 points that are in the fiducial volume are clustered and considered in the reconstruction
 781 process. First a charge threshold cut of 0.5 MeV is applied to all the remaining space points.
 782 This is to remove very low charge ghost points and reduce the overall number of points to
 783 cluster. The main goal of this step is to identify the large scale structure of the cosmic
 784 tracks in the data. Additionally, with a smaller number of space points the computational
 785 time for reconstruction is reduced.

786 The first stage of clustering uses BIRCH (balanced iterative reducing and clustering
 787 using hierarchies). The hyper parameters were tuned such that cosmic tracks are removed
 788 with minimal impact to showers involved from π^0 . Birch clustering was chosen because it
 789 scales well with large number of points, efficiently maintains large number of clusters in
 790 datasets and also handles outliers removal well. This clustering technique leverages on the
 791 inherent structure of charged particle tracks having a well define 3-dimensional trajectory.
 792 Particles such as protons, muons, and charged pions are continuously ionizing meaning
 793 that there should be not be gaps in the detected charge. This feature is much different than



(a) This figure shows an image of muon track as viewed from the BEE-WireCell image viewer.



(b) This figure shows an image of $\pi^0 \rightarrow \gamma\gamma$ decay as viewed from the BEE-WireCell image viewer.

794 EM-showers which have lots of gaps between detected charge. An example of this is shown
795 in figure 6.5

796 The next stage of the track and shower clustering process is to merge together proto-
797 clusters that did not get fully grouped together in the BIRCH clustering step. The second
798 pass clustering is geared toward larger object clustering. To address this, a 3D convex hull
799 is constructed around every cluster. Next, the euclidean distance between all the vertex
800 points are calculated. If the minimum merging distance is small, as it is for many charge
801 particle tracks, the clusters get merged together well. Clusters from showers, as they tend
802 to be very spread out, still need further merging.

803 The final stage of clustering is shower clustering. This requires there to be a distinction
804 between a cluster object that is shower-like or track-like. To do this, parameters that
805 describe various aspects of a cluster are calculated. The most important features from the
806 cluster parameters are cluster length and spread of the first principle component. More
807 details about track and shower selection are described later in section 6.6.

808 Once defined as a proto-shower cluster, a 3D charge weighted axis is fit to the cluster's
809 set of space points. The next step is to merge together proto-showers into their respective
810 showers. The goal for this step is to merge together proto-showers that originate from a

811 primary shower. To do this, a distance of closest approach (DOCA) for each proto-shower
 812 cluster axis pair is calculated along with the midpoint from the DOCA line for each pair.
 813 Next, a the closest distance from the midpoint to both showers are calculated. The angle
 814 between the two proto-shower axis is also calculated. A pair of proto-showers that have
 815 a DOCA that is less than 5 cm, an angle between 15 and 165 degrees, and both of the
 816 conversion lengths are less than 20 cm are merged together. The merging is done for all
 817 proto-shower cluster pairs as a final stage of the merging process.

818 6.6 Track and Shower Selection

819 6.6.1 Track Removal

820 For this analysis track removal is handled in a unique manner. The primary goal is to
 821 identify showers coming from a π^0 . Therefore, all cuts and optimizations will be tested
 822 against shower objects. Being that we simply are trying to identify charged tracks and not
 823 particle type, the charge information is not used. The general approach for track removal
 824 depends heavily on geometric properties such as length and linearity of the cluster.

825 6.6.2 Single π^0 Reconstruction

826 The vast majority (98.8%) of π^0 s decay into two photons. The relationship for the particle
 827 mass, which was defined in eq 6.1, shows the importance of properly accounting for the
 828 energy and angle between the decay photons. To understand a baseline for reconstruc-
 829 tion efficiency we have generated a sample of 10,000 single particle π^0 events isotropically
 830 throughout the detector volume with initial momenta spanning from 0 to 2 GeV.

831 First we will investigate energy deposited in detector from the decay. An plot of the true
 832 kinematic energy of photons from the decay particle is shown in Figure 6.3. It is important
 833 to note that both photons need to be reconstructed to form a mass. This means that we
 834 are driven to optimize the reconstruction to be robust around showers in the range of many
 835 tens of MeV in deposited energy. Photons that convert near the fiducial edge of the detector
 836 can escape and deposit only a small amount of energy in the detector. This poses problems
 837 for capturing the total amount of energy of the shower and drives the need for a fiducial

838 cut around the edges.

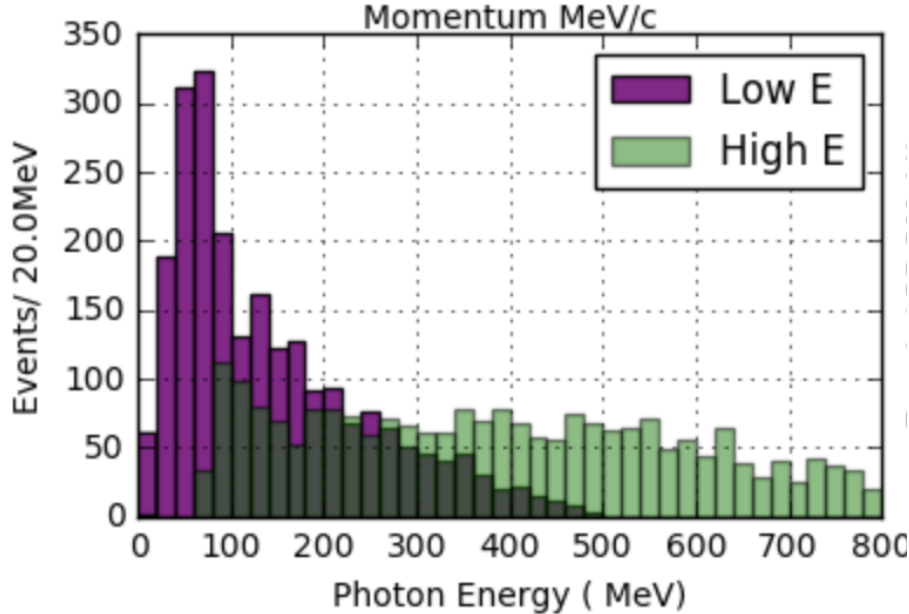
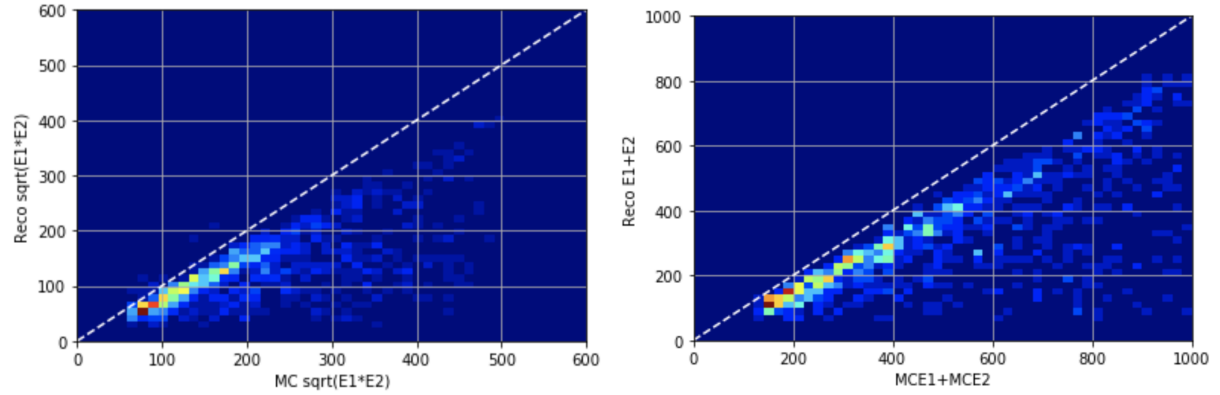


Figure 6.3: This figure shows the photon distribution for π^0 decays from a single particle sample of between 0-2 GeV. The higher energy photon is shown above in green along with the corresponding lower energy photon shown in magenta.

839 To understand the reconstruction accuracy for the energy we are most interested in two
840 metrics. The first is the total collected energy deposited by the two showers. This informs
841 us that we are accounting for most of the energy deposited and handling the fiducial cuts
842 well. The second is the product of the two shower energies. This directly impacts the
843 reconstructed mass resolution and informs us that we are clustering energy between the
844 two showers properly. In figure 6.4 both metrics are plotted for reconstruction against true.
845 Points along the diagonal would represent accurate model predictions. As we will see later
846 in this chapter, the energy product drives the width of the mass resolution.

847 Next we will investigate the effects of the opening angle between the two photons.
848 The minimum opening angle of the photons is constrained by the momentum boost as
849 the particle decays as shown in equation 6.3. The angular resolution is a very challenging
850 problem in LArTPC's using the traditional 2D projection approach. Fortunately, direct



(a) Scatter plot of reconstructed energy product vs true energy sum
(b) Scatter plot of reconstructed energy sum vs true energy product

Figure 6.4: Reconstructed energy sum and energy product for shower pairs. Both, the reconstructed energy sum and product is less than the true energy deposited.

851 3D reconstruction improves the angular resolution and allows for a better measurement of
852 shower direction.

$$\sin \frac{1}{2} \theta_{min} = \frac{M}{E_{\pi^0}} \quad (6.3)$$

853 A plot of the reconstructed vs true opening angle is shown in Figure 6.5. The $1 - \cos\theta$
854 term from equation 6.1 is sensitive to tails of the mass distribution.

855 Next, we apply a final set of selection cuts. First, we require that the distance of
856 closest approach between the two shower axis is less than 5 cm. This is to help ensure
857 that the photons are originating from a common origin. Next, we calculate the opening
858 angle between the two showers and require the angle to be within the range of 20 deg -
859 160 deg. Also, the photon conversion distance can not be longer than 70 cm for each of
860 the showers. This is done to help identify showers that are correlated from the same decay.
861 Finally we only accept showers that are above 50 MeV in reconstructed energy. Figure 6.6
862 shows the effect of various parameters as applied to the reconstruction. We find that the
863 deficit in mass peak is mainly due to the energy reconstruction. This is due to the missing
864 energy during clustering. For this analysis there is also an additional component of energy

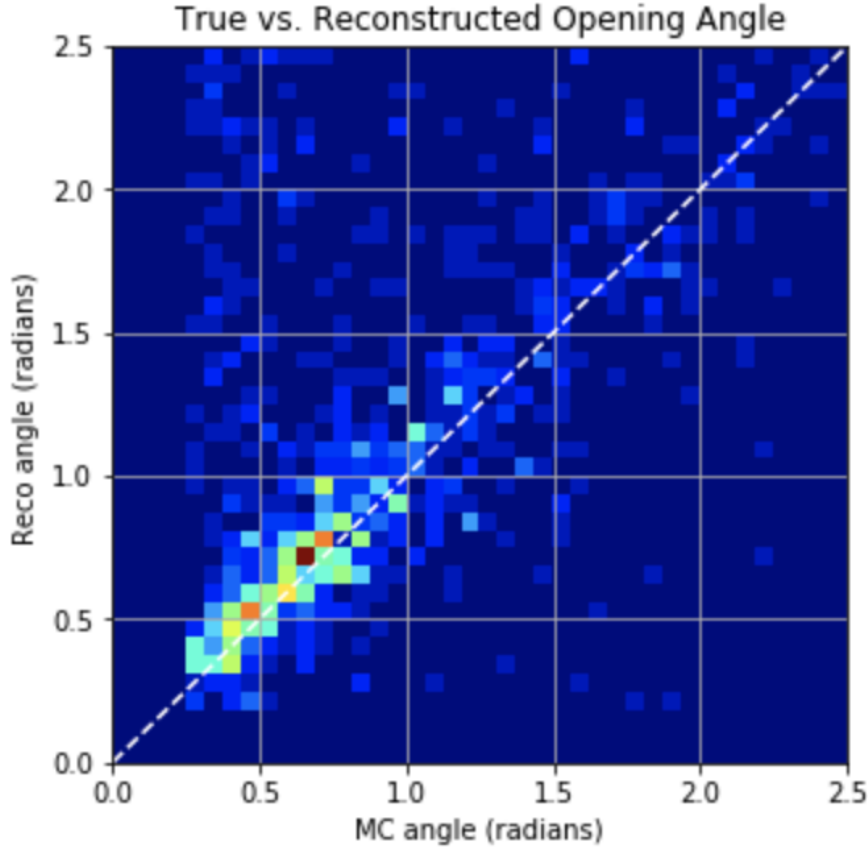


Figure 6.5: This scatter plot shows the reconstructed opening angle vs. true opening angle. We see that the reconstruction does very well with reconstructing this quantity due to the use of wire-cell's 3D approach. When the reconstruction performs badly it tends to identify small opening angles as large ones since we are not using any vertex information.

missing since we will not be using the initial t_0 -tag. The t_0 -tag is used to identify how far the electrons had to drift to reach the wire plane. Without using t_0 , there is no effective way to correct back for electron drift effects. Thankfully, this effect is can be captured in understanding the distribution of reconstructed mass peak in the Monte Carlo.

Finally, we address the overall efficiency for reconstruction. The average reconstruction efficiency between 0 and 1 GeV/c is 40.1%. The reconstruction efficiency is shown in Figure 6.7. As can be seen there, the efficiency drops at low and high energies. At low momentum the π^0 s are produced nearly at rest with both showers having similar energies.

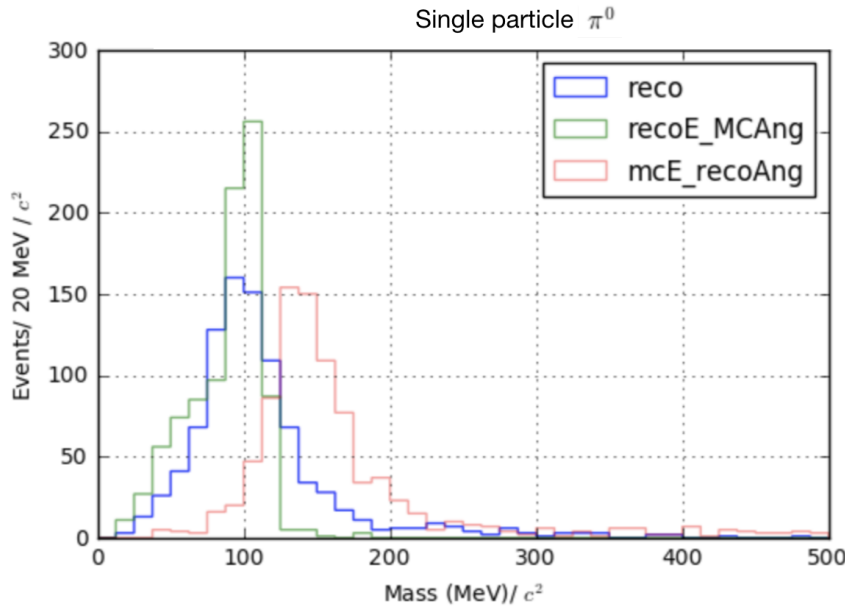


Figure 6.6: The reconstructed mass distribution is shown to highlight effects from reconstruction. First, in blue, the full reconstructed mass is shown. Second, in green, the reconstructed mass is calculated using the true angle. Third, in red, the reconstructed mass is calculated using the true energy.

873 Most importantly the showers are produced nearly back to back. Without having a well
 874 defined vertex, sometime the reconstruction will identify the angle as being close to zero.
 875 Being that there is a minimum opening angle cut some of the events are lost from this effect.
 876 At high momentum, many of the showers are boosted to small opening angle which we see
 877 a similar effect in the loss of efficiency.

878 6.7 Single π^0 cosmic sample

879 The MicroBooNE cosmis Monte Carlo is generated by CORSIKA (COsmic Ray Simulation
 880 for KAscade) v-7.4003[24]. CORSIKA simulates particles coming from a wide range of
 881 interactions initiated by cosmic ray particles in the upper atmosphere. The simulation is
 882 robust and accounts for various input parameters such as, longitude and latitude, elevation,
 883 and the earths magnetic field. The particles are simulated over a large region above the

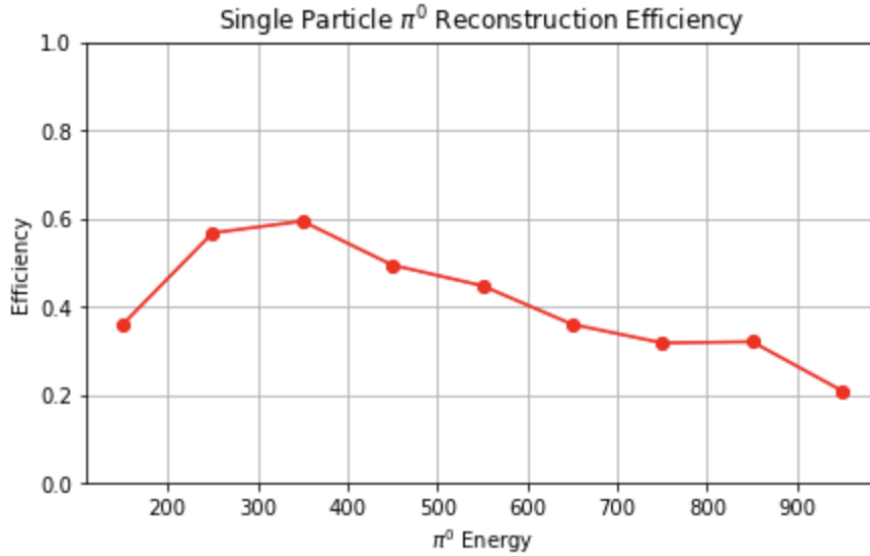


Figure 6.7: The plot shows the π^0 reconstruction efficiency for π^0 s over a 1,000-10,000 MeV energy range. The reconstruction efficiency peaks around 350 MeV which conveniently is around the production energy for cosmic π^0

884 detector complex but only particles that travel through the detector cryostat volume are
 885 kept. The passage of these particles is simulated by the GEANT4 package. Cosmic rays
 886 that do not travel through the cryostat have a low likelihood of producing secondary or
 887 tertiary particles that enter the detector TPC volume [25].

888 In one MicroBooNE drift window (2.3ms) there are on average 6 cosmic muons. The
 889 muons do not directly contribute to many EM-showers but sometimes pass through an EM-
 890 shower from another particle. For MicroBooNE, the vast majority of muons are through
 891 going and do not lead directly to any method of π^0 production.

892 Various other particles such as, protons, neutrons, and charged pions enter the TPC
 893 volume and may produce π^0 s. A distribution of π^0 production process is shown in Figure
 894 6.8. Nearly half of the π^0 s produced in the MicroBooNE TPC are produced through neutron
 895 inelastic scattering.

896 In total, 90,297 CORSIKA truth events were produced to constrain production rates for
 897 signal and background. From that, a random sample of 10K events were ran through the
 898 wire-cell imaging reconstruction. Additionally, a signal sample of events which contain a

899 single neutron π^0 of $\approx 1.2\text{K}$ was produced and reconstructed through the wire-cell imaging.
 900 The exact rates will be discussed in Chapter 7.

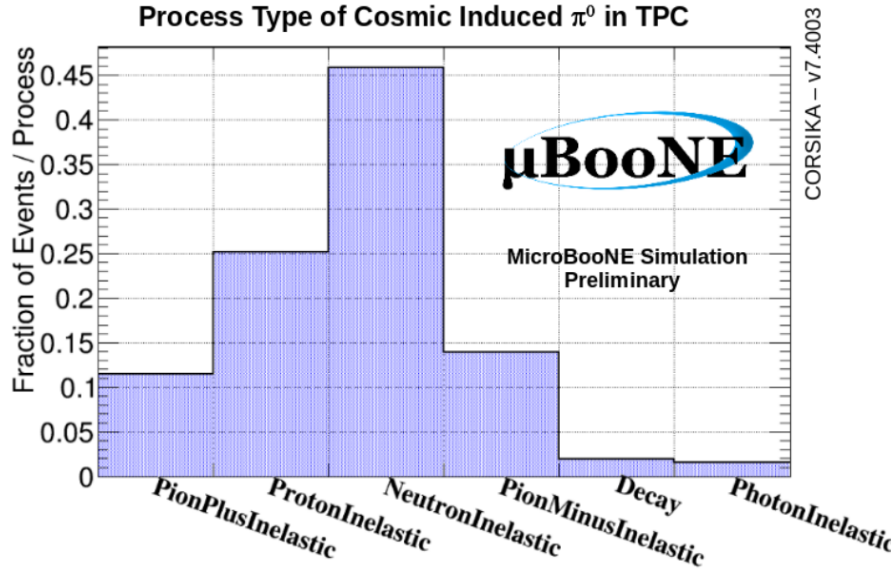


Figure 6.8: Physical process for cosmic π^0 that decay inside the TPC.

901 MircoBooNE, being a surface detector, has very minimal shielding from cosmic rays.
 902 Most of the π^0 s coming from protons and charge pions do not make it very far into the
 903 detector fiducial volume due to hadronic interactions outside the detector. The building
 904 and cryostat easily absorb and re-scatter hadronic particles. This coupled with the argon
 905 that is above the TPC provide reduction in charged hadronic particles that make it to the
 906 fiducial volume. The neutrons do not interact as much and are slightly more distributed
 907 over the TPC fiducial volume. A stacked scatter plot is shown in figure 6.9

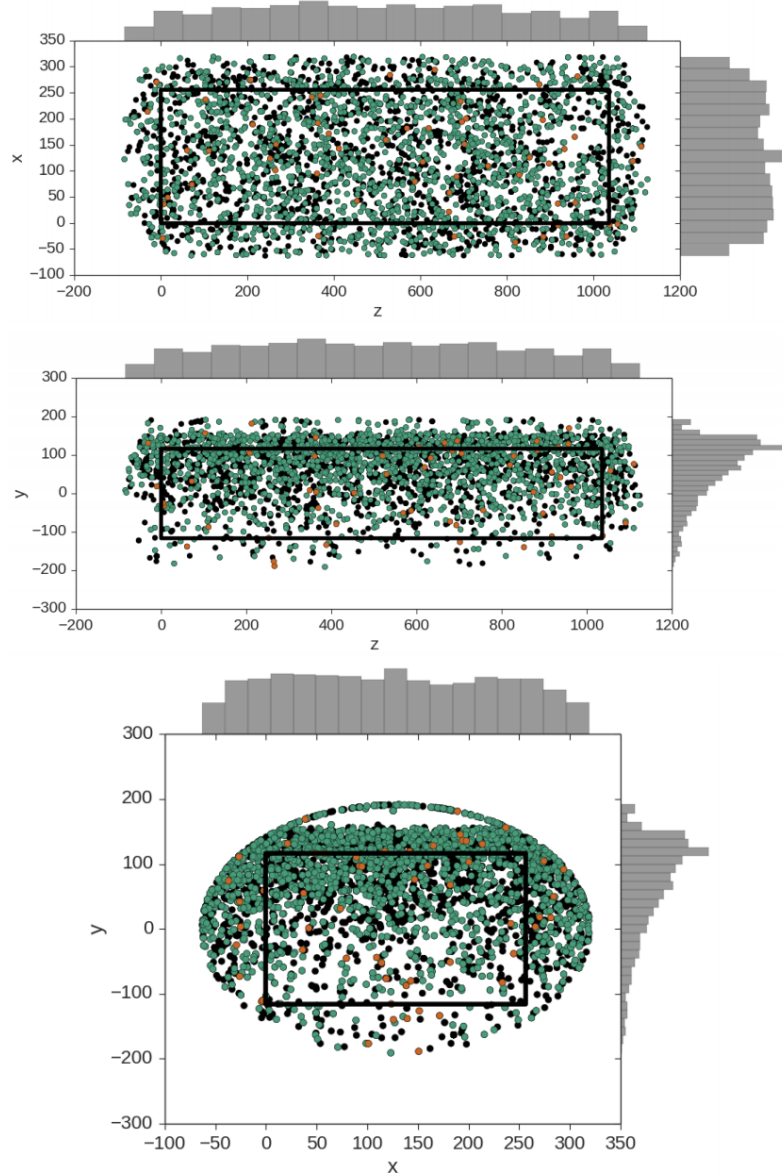


Figure 6.9: These plots show the decay point of actual cosmic π^0 s throughout any time in the 4.8 ms window. The green points represent neutron induced π^0 s, the orange represent photon induced π^0 s, and the black represent a π^0 that was produced from a charged particle. In each plot the black box is to represent the entire TPC dimensions not including fiducial cuts. Note that this is a stacked scatter plot with ordering; charged particle (black), photon (orange), neutron (green) from bottom to top.

Chapter 7

Results

The goal of this study is primarily two fold. The first goal is to highlight a different technique to reconstruct π^0 and EM-showers in an LArTPC. To best showcase this reconstruction technique we will focus on reconstructing π^0 s that are induced from a single neutron. In many instances, neutral induced interactions do not have a visible vertex. Reconstructing EM showers from a π^0 decay without a vertex poses many challenges for traditional techniques. The Wire-Cell imaging approach allows for a full 3D shower reconstruction without the use of a vertex. The second goal is to measure and compare the cosmic ray neutron induced $1-\pi^0$ production rate in the MicroBooNE detector. This reconstruction technique is well suited for this type of analysis.

This section will address results from both Monte Carlo and actual MicroBooNE cosmics data. To be clear, we will define our signal to be events that produce 1 and only 1 neutron induce single π^0 inside the TPC fiducial volume. For this analysis the fiducial volume is defined from: X [0 cm, 256 cm] , Y[-116 cm, 116 cm], Z[400 cm, 800 cm]. We also restrict our bounds to events that happen in 1 drift window as defined in section 6.7 .

7.1 Monte Carlo Simulation

First, a word on simulation constraints. While the wire-cell imaging process provides considerable gains towards extracting high resolution LArTPC reconstruction, it does come with a high computational cost. This was an issue for generating a large sample of Monte

Table 7.1: CORSIKA MC rates

Neutron induced 1 π^0	1,255
Neutron induced 1 π^0 outside	13,434
Proton induced 1 π^0	5,038
Other induced 1 π^0	9,530
no 1 π^0 or multi π^0	61,040

928 Carlo for Wire-Cell imaging. The process should be able to be distributed, but for this anal-
 929 ysis it this process was not yet available. This required us to use an up-sampling technique
 930 with the background Monte Carlo sample which is describe in the subsequent paragraphs.

931 First a enhanced sample of 1,255 signal events were generated from CORSIKA, processed
 932 through wire-cell imaging, and reconstructed with the described process in section 6. A
 933 background only sample, consisting of 8,720 randomly sampled background events were
 934 processed through wire-cell imaging and the reconstruction. This number was then scaled by
 935 0.0139 to obtain an absolute background value relative to the enhanced signal sample. This
 936 scaling represents a new total of 90,297 events. One event corresponds to one MicroBooNE
 937 readout frame.

938 From the total sample we find that 1.39% are signal. The remaining background is
 939 divided into 5 categories: (1) neutron induced events that are produced outside the fiducial
 940 volume, (2) proton induced events that produce 1 π^0 either inside or outside the fiducial
 941 volume, (3) Events that produce 1 π^0 either inside or outside the fiducial volume not coming
 942 from a proton or neutron, (4) Multi π^0 produced either inside or outside the fiducial volume,
 943 (4) Events that do not contain any π^0 . Table 7.1 shows the corresponding counts from the
 944 90,297 CORSIKA sample.

945 Next, the selection cuts described in chapter 6 are applied to both the signal sample and
 946 Monte Carlo. There are a total of 443 events that pass the cuts made in section 6. This
 947 corresponds to a signal efficiency of 35.9%. A plot for the reconstructed mass is shown in
 948 figure 7.1. The mass peak, which is supposed to be around $135 \text{ MeV}/c^2$, is centered around
 949 $100 \text{ MeV}/c^2$ due to the missing energy. This is in agreement with what we expect from the
 950 single particle π^0 studies from section 6.

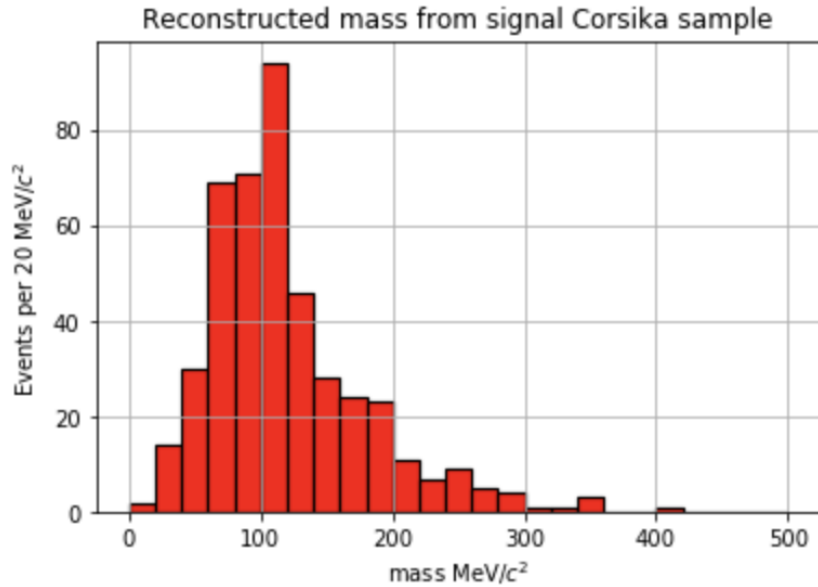


Figure 7.1: Plot of the mass distribution for MC neutron induced signal events.

951 Then, the same cuts were applied to the background only sample. We find there to be
 952 a background rate of 2.3%. Ultimately resulting in a signal:background of 0.21 (Approximate-
 953 mately 1 : 5.6). A plot of the reconstructed mass distribution for the entire background is
 954 shown in figure 7.2

955 It is important to note that the background distribution will also contain π^0 events. The
 956 background distribution as described in section 7.1 is plotted in figure 7.2. The distribution
 957 should also have some well reconstructed π^0 . For this analysis, since we did not require the
 958 use of a vertex there is a sizable portion of background that are actual reconstructed π^0 .
 959 This comes from two primary effects both of which are products of how the reconstruction
 960 criteria is defined. The first effect is part of the group coming from events with "No π^0 "
 961 group. Many of the events are actual π^0 particles but reconstructed out side of the fiducial
 962 volume. The second effect is in the remaining π^0 groups which obviously contains at least
 963 one π^0 . Being that we remove as many track as possible, Many proton and charged pion
 964 tracks are removed. The in eyes of the selection process a proton or charged pion induced
 965 π^0 event has a near identical topology to the signal.

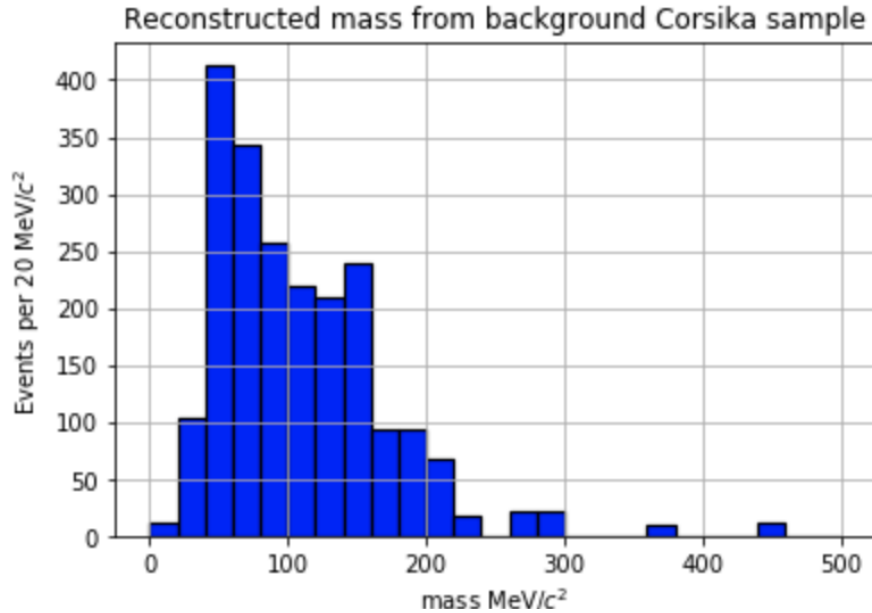


Figure 7.2: Plot of the mass distribution for MC cosmic background events.

966 7.2 Data

967 The same selection cuts were applied to a dataset of 13,022 off beam cosmic data events
 968 that were sampled from the 'MicroBooNE Good Run List'. This is an internal list that
 969 MicroBoone generates to define when the detector is in acceptable running mode. This list
 970 takes into account various aspects of the detector such as wire stability, argon purity, PMT
 971 response, etc. It is important to note that the data sample that is used in this thesis is only
 972 from the good run list. Doing this, assumes that any bias in the sample is averaged over
 973 for interaction type. The mass distribution is calculated from the given 13,022 sample and
 974 there is a clear mass peak from the π^0 s that is also centered below the actual $135 \text{ MeV}/c^2$
 975 mass.

976 7.3 Data-Monte Carlo Comparison

977 To better understand the data distribution, we first plot an area normalized histogram for
 978 Monte Carlo and Data. This is shown in figure 7.3. We see that the shape is indeed similar
 979 but not ideal. Given this, the area normalized shape comparison only serves the purpose of

980 showing that we believe we are reconstructing π^0 's and reasonably handling the background.

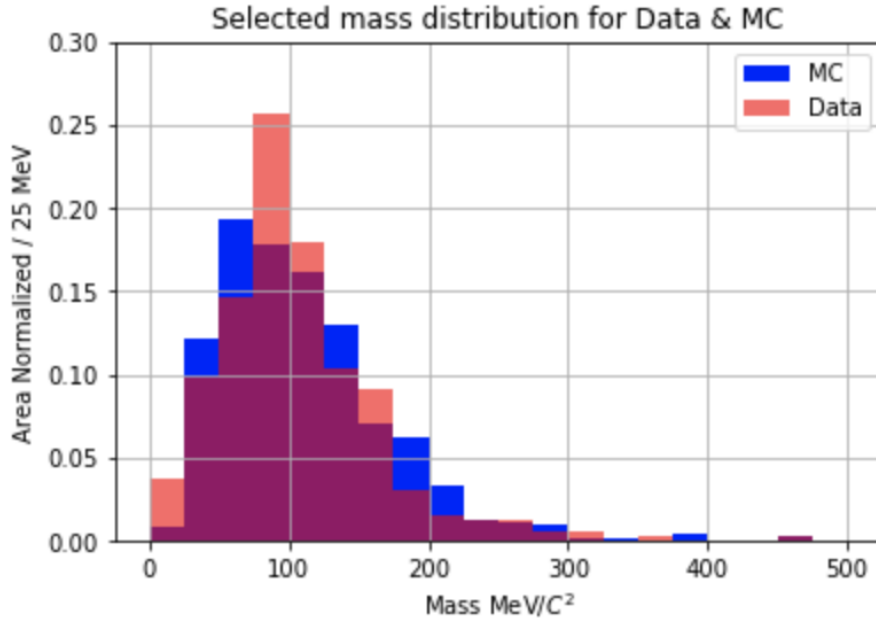


Figure 7.3: Area normalized Data-Monte Carlo mass distributions. The shapes between the data and Monte Carlo distributions provide confidence that we are reconstructing π^0 's in the distribution.

981 To better compare data and Monte Carlo an absolute rate comparison should be made.
 982 This will address how well the Monte Carlo represents the data. The mass distribution is
 983 shown in Figure 7.4. Out of the box, CORSIKA slightly over predicts the rate from data
 984 producing χ^2/df of 1.37. To address this, a χ^2 minimization can be performed fit the Monte
 985 Carlo to the data. Both the signal and background are varied to optimize the fit to data.
 986 We will assume a flat 5% systematic error and account for the statistical error of both the
 987 Monte Carlo and data. We find that the fit returns a minimum of 0.73 χ^2/df when the
 988 signal is reduced by 72% and the background is also reduced by 84%. The adjusted mass
 989 distribution from the fit is shown in Figure 7.5

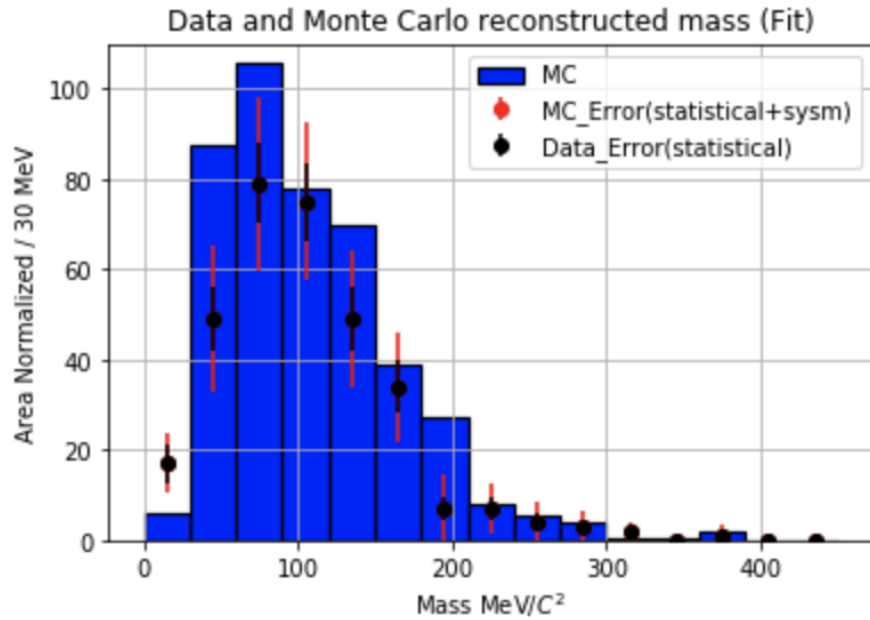


Figure 7.4: This plot shows the mass distribution from data with respect to the unchanged Monte Carlo.

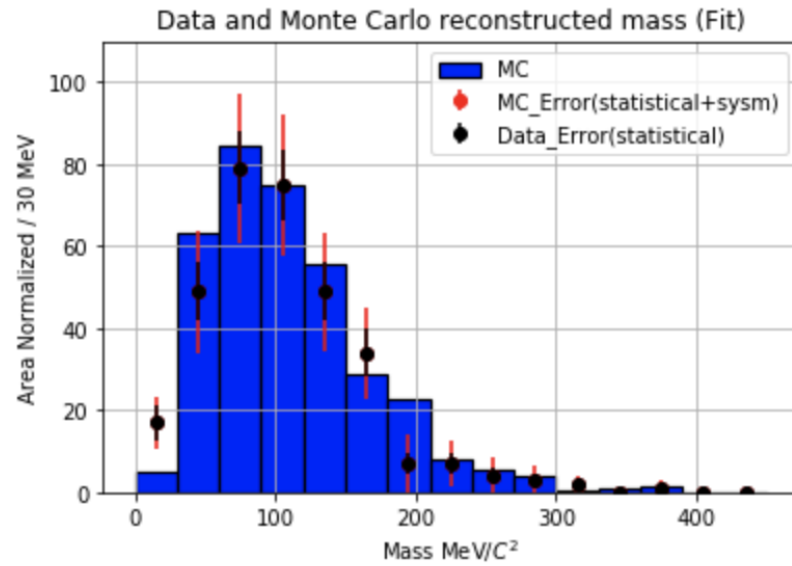


Figure 7.5: This plot shows the mass distribution from data with respect to the fitted Monte Carlo.

990 Chapter 8

991 Conclusions

992 8.1 Conclusion

993 The construction of MicroBooNE is an essential step forward for the low energy neutrino
994 physics community. The R&D process provided valuable insights towards future LArTPC
995 detector technology. The MicroBooNE detector was completed in 2015 and has since been
996 collecting valuable data.

997 This thesis showcases a radically new technique for 3D reconstruction of EM showers.
998 Although wire-cell does require a high amount of computational resources, the improved
999 3D reconstruction capabilities for EM showers provide justification. Additionally, we are
1000 able to reconstruct π^0 s without the use of vertex information. We have built an algorithm
1001 to identify neutron induced single π^0 events. We found that the current CORSIKA Monte
1002 Carlo slightly over predicts the rate of neutron induced π^0 in the MicroBooNE detector.
1003 The data used in this thesis is entirely on cosmic ray data but the extension to a neutral
1004 current single π^0 interaction is the next logical step.

Part I

Appendices

SP0TER is located on Github:

¹⁰⁰⁷
https://github.com/1grossora>Show_Sp0ter

To obtain a copy of the code you first must have git installed. Next clone the repository to a location of your choice by using the command below.

```
git clone git@github.com:1grossora>Show_Sp0ter.git
```

The requirements are located on the readme page above. Base Requirements:

- Root version: 6.05 or greater
- scipy, numpy, sklearn
- Cython

MC or data from MicroBooNE (not public). A list of important parameters are listed below. The values of these parameters were used for this thesis study but can be varied as the users discretion. More documentation can be found on the github repository page listed above.

Parameter Name	Parameter Value	Location	Parameter Description
charge_thres	500	Utils	Threshold value corresponding to wirecell space point charge
nq_thresh	600	Utils	Max number of charge points in a wirecell blob
zlo	400	Utils	Lower bound z distance
zhi	800	Utils	Upper bound z distance
ylo	116	Utils	Lower bound y distance
yhi	-116	Utils	Upper bound y distance
xlo	-1000	Utils	Lower bound x distance
xhi	1000	Utils	Upper bound x distance
make_json	False	Utils	Produce a json for the BEE display
mincluster	20	Reco	Minimum amount of space points

			needed	65
nn_dist ₁₀₀₈	2	Reco	Minimum distance required for a space point to be merged	
birch_leaf	1000	Reco	Max size of a cluster from birch clustering	
birch_min_cluster	20	Reco	Minimum size of a cluster from birch clustering	
edge_dist	1	Merge	Distance require to merge together hulls from birch clusters	
stitch_mincluster	100	Merge	Minimum number of space points requires to be considered a cluster after stitching	
vari_0	0.9985	Track	Value of the first charge weighted pca of the cluster	
ts_fcl_length	20	Track	Minimum length of hull to designate as a shower	
ts_fcl_minsize	10	Track	Minimum size of the hull to designate as a shower.	
Doca_sweep	10	Shower	Minimum length between two end points of two clusters	
lcmin	25	Shower	Minimum length showers for a final merged shower	
vari_1	0.998	Shower	Value of the second charged weighted PCA of the cluster	
ts_scl_length	25	Shower	Minimum length of shower	
ts_scl_minsize	10	Shower	Minimum volume of the size of showers	
snn_dist	2	Shower	Final showers within this distance are merged.	

Bibliography

- [1] Henri becquerel biography. 2014.
- [2] W. Pauli. Open letter to the group of radioactive people at the gauverein meeting in tubingen. 1930.
- [3] S. Schael et al. Precision electroweak measurements on the Z resonance. *Phys. Rept.*, 427:257–454, 2006.
- [4] C. Patrignani et al. Review of Particle Physics. *Chin. Phys.*, C40(10):100001, 2016.
- [5] D. DeCamp and B. Deschizeaux et al. Determination of the number of light neutrino species. *Physics Letters B*, 231(4):519 – 529, 1989.
- [6] C. Rubbia. The Liquid Argon Time Projection Chamber: A New Concept for Neutrino Detectors. 1977.
- [7] S. Amerio and S. Amoruso. et al. Design, construction and tests of the icarus t600 detector. *Nuclear Instruments and Methods in Physics Research Section A: Accelerators, Spectrometers, Detectors and Associated Equipment*, 527(3):329 – 410, 2004.
- [8] C. Anderson et al. The ArgoNeT Detector in the NuMI Low-Energy beam line at Fermilab. *JINST*, 7:P10019, 2012.
- [9] H. Chen et al. A Proposal for a New Experiment Using the Booster and NuMI Neutrino Beamlines: MicroBooNE.
- [10] A. A. Aguilar-Arevalo et al. Observation of a Significant Excess of Electron-Like Events in the MiniBooNE Short-Baseline Neutrino Experiment. 2018.

- 1029 [11] Pip Hamilton. First Measurement of Neutrino Interactions in MicroBooNE. In *18th*
1030 *International Workshop on Neutrino Factories and Future Neutrino Facilities Search*
1031 (*NuFact16*) *Quy Nhon, Vietnam, August 21-27, 2016*, 2016.
- 1032 [12] The microboone technical design report. 2012.
- 1033 [13] R. Acciarri et al. Design and Construction of the MicroBooNE Detector. *JINST*,
1034 12(02):P02017, 2017.
- 1035 [14] Teppei Katori. The MicroBooNE light collection system. *JINST*, 8:C10011, 2013.
- 1036 [15] Costas Andreopoulos, Christopher Barry, Steve Dytman, Hugh Gallagher, Tomasz
1037 Golan, Robert Hatcher, Gabriel Perdue, and Julia Yarba. The GENIE Neutrino Monte
1038 Carlo Generator: Physics and User Manual. 2015.
- 1039 [16] A. A. Aguilar-Arevalo et al. The Neutrino Flux prediction at MiniBooNE. *Phys. Rev.*,
1040 D79:072002, 2009.
- 1041 [17] A. Aguilar-Arevalo et al. Evidence for neutrino oscillations from the observation of anti-
1042 neutrino(electron) appearance in a anti-neutrino(muon) beam. *Phys. Rev.*, D64:112007,
1043 2001.
- 1044 [18] A. A. Aguilar-Arevalo et al. The MiniBooNE Detector. *Nucl. Instrum. Meth.*, A599:28–
1045 46, 2009.
- 1046 [19] A. A. Aguilar-Arevalo et al. Unexplained Excess of Electron-Like Events From a 1-GeV
1047 Neutrino Beam. *Phys. Rev. Lett.*, 102:101802, 2009.
- 1048 [20] A. Ankowski et al. Energy reconstruction of electromagnetic showers from pi0 decays
1049 with the ICARUS T600 Liquid Argon TPC. *Acta Phys. Polon.*, B41:103–125, 2010.
- 1050 [21] J. S. Marshall and M. A. Thomson. The Pandora Software Development Kit for Pattern
1051 Recognition. *Eur. Phys. J.*, C75(9):439, 2015.
- 1052 [22] R. Acciarri et al. Convolutional Neural Networks Applied to Neutrino Events in a
1053 Liquid Argon Time Projection Chamber. *JINST*, 12(03):P03011, 2017.

- 1054 [23] Xin Qian, Chao Zhang, Brett Viren, and Milind Diwan. Three-dimensional Imaging
1055 for Large LArTPCs. *JINST*, 13(05):P05032, 2018.
- 1056 [24] D. Heck, G. Schatz, T. Thouw, J. Knapp, and J. N. Capdevielle. CORSIKA: A Monte
1057 Carlo code to simulate extensive air showers. 1998.
- 1058 [25] S. Agostinelli et al. GEANT4: A Simulation toolkit. *Nucl. Instrum. Meth.*, A506:250–
1059 303, 2003.